Petroleum Science 22 (2025) 4341–4356

Contents lists available at ScienceDirect

Petroleum Science

journal homepage: www.keaipublishing.com/en/journals/petroleum-science

Original Paper

Effects of natural fractures in cap rock on CO_2 geological storage: Sanduo Formation and Dainan Formation of the early Eocene epoch in the Gaoyou Sag of the Subei Basin

Yun-Zhao Zhang [a,b,*], Quan-Qi Dai [c,d,e,**], Lian-Bo Zeng [f], Rui-Qi Li [g], Rong-Jun Zhang [h,i], Le Qu [h,i], Yang-Wen Zhu [c,d,e], Hai-Ying Liao [c,d,e], Hao Wu [j]

[a] School of Earth Sciences and Engineering, Xi'an Shiyou University, Xi'an, 710065, Shaanxi, China
[b] Shaanxi Key Laboratory of Petroleum Accumulation Geology, School of Earth Sciences and Engineering, Xi'an Shiyou University, Xi'an, 710065, Shaanxi, China
[c] State Key Laboratory of Shale Oil and Gas Enrichment Mechanisms and Efficient Development, Beijing, 102206, China
[d] Petroleum Exploration and Development Research Institute, SINOPEC, Beijing, 102206, China
[e] SINOPEC Key Laboratory of Carbon Capture, Utilization and Storage, Beijing, 102206, China
[f] College of Geosciences, China University of Petroleum (Beijing), Beijing, 102249, China
[g] Research Institute of Exploration and Development, PetroChina Changqing Oilfield Branch Company, Xi'an, 710018, Shaanxi, China
[h] College of Petroleum Engineering, Xi'an Shiyou University, Xi'an, 710065, Shaanxi, China
[i] Xi'an Key Laboratory of Tight Oil (Shale Oil) Development, Xi'an Shiyou University, Xi'an, 710065, Shaanxi, China
[j] China Key Laboratory of Mineral Resources in Western China, School of Earth Sciences, Lanzhou University, Lanzhou, 730000, Gansu, China

ARTICLE INFO

Article history:
Received 27 March 2024
Received in revised form
19 March 2025
Accepted 2 August 2025
Available online 7 August 2025

Edited by Xi Zhang and Jie Hao

Keywords:
Cap rock
Natural fractures
CO_2 geological storage

ABSTRACT

During the CO_2 injection and geological storage process, the integrity of the cap rock significantly influences the long-term safety of CO_2 storage. Natural fractures within the cap rock serve as potential pathways for CO_2 migration, thereby increasing the risk of CO_2 leakage. In this study, we determined the types, developmental characteristics, permeability changes, and CO_2-H_2O-Rock reactions of natural fractures in the mudstone cap rocks of the Sanduo Formation (E_3s) and Dainan Formation (E_2d) in the Gaoyou Sag of the Subei Basin using core observations, thin-section analysis, rock mechanics experiments, and paleomagnetic directional analysis. We identified four tectonic fracture sets (NNW, NWW, EW, and NE); high-angle shear fractures, ranging from 60° to 90° (average 82°) and typically measuring 4–12 cm (average 7.5 cm), dominate the assemblage, while slip fractures, ranging from 32° to 50° (average 36°) and measuring 3–6 cm (average 3.9 cm), are also present. At the microscale, shear fractures average 160 μm, and bedding fractures average 82 μm. Notably, 85.78% of shear fractures are unfilled, with calcite filling observed in 14.22%, while other fracture types show no filling. Permeability tests on samples without fractures reveal that permeability declines rapidly below 9 MPa, especially in shallower samples, followed by a slower reduction between 9 and 13 MPa, and ultimately stabilizes at approximately 0.00003 mD. In contrast, samples with fractures exhibit permeability that is 3–4 orders of magnitude higher; their fracture permeability decays according to a power law with pressure yet remains above 10 mD even at 46 MPa. Fractures with larger dip angles and those aligned with the maximum principal stress demonstrate the highest permeability. While silicate-filled fractures exhibit negligible changes in permeability, carbonate-filled fractures experience a temporary enhancement due to dissolution; however, subsequent permeability remains controlled by factors such as effective stress and fracture orientation.

1. Introduction

The rapid development of the world economy has led to increasingly prominent environmental and climate issues, such as global temperature rise, rising sea levels, and extreme natural

* Corresponding author.
** Corresponding author.
E-mail addresses: zhangyunzhaocup@163.com (Y.-Z. Zhang), daiqq.syky@sinopec.com (Q.-Q. Dai).

Peer review under the responsibility of China University of Petroleum (Beijing).

https://doi.org/10.1016/j.petsci.2025.08.002

disasters (Dar et al., 2022; Sennaoui et al., 2025). Currently, approximately 140 government organizations worldwide have committed to achieving net-zero carbon emissions, and the vision of carbon neutrality has become a global consensus (Ishaq and Crawford, 2023; Li et al., 2023b). The carbon emissions from the combustion of fossil fuels account for 33%–40% of the total global carbon emissions generated by human activities (Khatri et al., 2006; Liu et al., 2024). Due to the increasing global population and the accelerated industrialization process, there remains a strong dependence on fossil energy on a global scale for an extended period, and the demand for energy is expected to continue to rise (Sakthivel et al., 2024; Xu et al., 2023). Amidst the prominent contradiction between human development needs and climate and environmental concerns, Carbon Capture, Utilization, and Storage (CCUS) technology has become a more favorable option for achieving decarbonization goals due to its low implementation risks and uncertainties (Liu et al., 2023; Zhao et al., 2025). CO_2 storage is a crucial component of CCUS, and geological storage sites include depleted oil and gas reservoirs, unmineable coal seams, deep-sea locations, and deep saline aquifers (Chen et al., 2022; Li et al., 2023a; Yekeen et al., 2020). In particular, depleted oil and gas reservoirs serve as natural storage sites for CO_2. They possess well-contained systems and substantial storage capacity, ensuring high safety in the medium to long term. Additionally, by enhancing oil and gas recovery rates, operators can gain additional economic returns. Thus, depleted oil and gas reservoirs are considered ideal and economically viable locations for CO_2 geological storage (Bao et al., 2023; Wang et al., 2017). However, there is always a risk of leakage associated with the storage of CO_2 in depleted oil and gas reservoirs, as well as other geological storage methods (Bachu, 2016; Yang et al., 2023). If there is a large-scale, short-term leakage of stored CO_2, it could potentially lead to more severe natural disasters (Bachu and Adams, 2003; Hou et al., 2022). A low-permeability cap rock above the CO_2 reservoir is essential for effective CO_2 containment (Li et al., 2006). Therefore, the assessment of the cap rock in the target area for CO_2 geological storage is a fundamental task to ensure the long-term secure storage.

The cap rock is a low-permeability sealing layer, such as mudstone, salt, or gypsum, directly overlaying the reservoir. The degree of its sealing directly influences the safety and stability of long-term CO_2 storage (Smith, 1966; Song and Zhang, 2013). The sealing mechanisms of cap rock include capillary sealing, overpressure sealing, and hydraulic sealing. Capillary sealing involves capillary pressure in the cap rock pores hindering fluid escape, and the sealing capability depends on the capillary pressure (P_c) (Al-Yaseri et al., 2022; Bachu et al., 2007). It is primarily influenced by the diagenetic evolution of mudstone cap rock, interfacial tension, wettability, and cap rock thickness (Ali et al., 2022; Tremosa et al., 2017). The overpressure sealing of the cap rock is mainly controlled by the adsorption resistance in the cap rock pores, and the sealing capability enhances with an increase in overpressure (Hao et al., 2015). The capillary pressure of hydraulic sealing in the cap rock is exceptionally high, and underground water in the cap rock blocks the diffusion and migration of fluids driven by static hydraulic pressure or gravity (Chen et al., 2023a; Finkbeiner et al., 2001). The diffusion and permeation patterns of fluids in porous media indicate that the pore network and natural fractures directly determine the permeability of the cap rock and the diffusion capacity of CO_2 (Ichikawa et al., 2007). Changes in the cap rock permeability significantly affect its sealing effectiveness and the ability for underground CO_2 storage (Zhang et al., 2021a). After underground injection of CO_2, changes in the permeability of cap rock pores may lead to CO_2 leakage through the following two processes: (1) Mechanical damage. Following the injection of CO_2 into the underground target layer, the pressure gradient in the target layer moves upward (Rohmer et al., 2016). The occurrence of changes in interfacial tension, wetting contact angles, and pore throat radii between cap rock fluids and CO_2 makes it highly susceptible to the formation of preferential flow channels, leading to capillary leakage (Edlmann et al., 2013; Ma et al., 2020). (2) Chemical reactions. After CO_2 injection into the underground target layer, it forms carbonic acid fluid with groundwater, and acidic fluid tends to migrate upward to the bottom of the cap rock (Bachu and Shaw, 2003; Grimm et al., 2012). Subsequently, physical and chemical reactions occur with minerals in the cap rock, leading to mineral dissolution, new mineral precipitation, and pore plugging, thereby enhancing or reducing the sealing capability of the cap rock (Hou et al., 2022; Rohmer et al., 2016). In summary, after the injection of CO_2 (Asem and Gardoni, 2022; Chen et al., 2023a), changes in pressure, stress fields, and CO_2-H_2O-Rock interactions within the cap rock result in corresponding alterations in the sealing effectiveness of the cap rock (Rutqvist and Tsang, 2002; Zheng and Espinoza, 2021). Simultaneously, after CO_2 injection, the impact of natural fractures on the permeability of the cap rock and CO_2 geological storage cannot be ignored.

Natural fractures refer to macroscopic discontinuity surfaces that exist in rocks, formed due to tectonic deformation or physical diagenetic processes (Cao et al., 2024; Zeng et al., 2013; Zhang et al., 2021b). Under the influence of tectonic stress during geological history, both cap rock and reservoir may develop natural fractures to varying degrees (Ju et al., 2019; Zeng, 2008). Over the years, due to the significance of natural fractures as crucial reservoir storage space and primary fluid flow pathways, scholars have focused on systematic research into the types, formation mechanisms, and controlling factors of reservoir fractures (Zeng et al. 2023, 2024). This has led to the development of a series of characterization methods and prediction techniques (Ju and Sun, 2016; Laubach et al., 2019). The natural fractures within the cap rock represent potential pathways for CO_2 migration, and the presence of natural fractures always increases the risk of CO_2 leakage (Antropov et al., 2017). After the injection of CO_2 into the underground target layer, the increase in pore fluid pressure can reactivate natural fractures or induce new fractures in the cap rock, disrupting hydraulic sealing and leading to CO_2 leakage (Rui et al., 2025). In process (1), if natural fractures exist within the cap rock, mechanical damage becomes more severe, leading to several orders of magnitude increase in the cap rock permeability (Elkhoury et al., 2013). This can even result in changes in the stress and rock mechanics properties of the cap rock, leading to its collapse (Durham et al., 2001). Simultaneously, in process (2), CO_2-H_2O-Rock interaction can alter the structure and permeability of fractures, affecting the sealing integrity of the cap rock (Wu et al., 2017). Surprisingly, there is little knowledge about the impact of natural fractures in the cap rock on CO_2 geological storage based on the study of the characteristics and distribution patterns of natural fractures.

In this study, we focus on the cap rock of the Paleogene Sanduo Formation and Dainan Formation in the Gaoyou Sag of the Subei Basin. Firstly, through core drilling and scanning electron microscopy data, we identified the types of natural fractures in the cap rock, characterized important parameters such as fracture dip, density, length, and effectiveness, and combined them with core magnetic orientation technology to determine the orientation of fractures, collectively elucidating the development characteristics of cap rock fractures. Secondly, through rock mechanics experiments and physical property tests, we clarified the opening pressure and permeability of cap rock fractures. Finally, we analyzed the factors influencing the opening pressure of cap rock fractures during CO_2 injection and their impact on CO_2 geological storage,

and discussed the factors influencing the permeability of cap rock fractures after CO_2 injection and their impact on CO_2 geological storage.

2. Geological settings

2.1. Location and structure

Subei Basin is a Cenozoic rift basin formed above the Cretaceous basement. It is the onshore part of the Northern Jiangsu-South Yellow Sea Basin, with an area of approximately 35,000 km^2 (Fig. 1(a) and (b)) (Quaye et al., 2019). The basin trends northeastward, bounded by the Tan-Lu Fault to the west, connected to the SuLu Orogenic Belt to the north, extending eastward into the Yellow Sea, and delimited to the south by the Yangzhou-Rugao. After the early extensional faulting stage, late subsidence stage, and sagging stage, the basin formed successively from north to south, including the Yanfu Depression, Jianhu Uplift, and Dongtai Depression (Liu et al., 2016). The Gaoyou Sag is located in the southern part of the Subei Basin, generally trending northeast (Fig. 1(c)). It has a width of approximately 25–35 km from north to south, a length of about 100 km from east to west, and covers an area of approximately 2670 km^2. The southern part of the sag is adjacent to the Tongyang Uplift and Wubu Low Uplift, while the northern part is connected to the Zheduo Low Uplift by a gentle slope. In the west, it is connected to the Jinhu Sag through a saddle between the Liubu Low Uplift and the Lingtangqiao Low Uplift. To the east, it is bordered by the Baiju Depression. Formed during the Late Cretaceous Yezheng Movement and the Cenozoic Wubu Movement, the depression exhibits a characteristic funnel shape with a steep southern slope and a gentle northern slope (Zhu et al., 2023b). From south to north, the sag can be further divided into the southern steep slope zone, the central deep sag zone, and the northern slope zone (Fig. 1(d)).

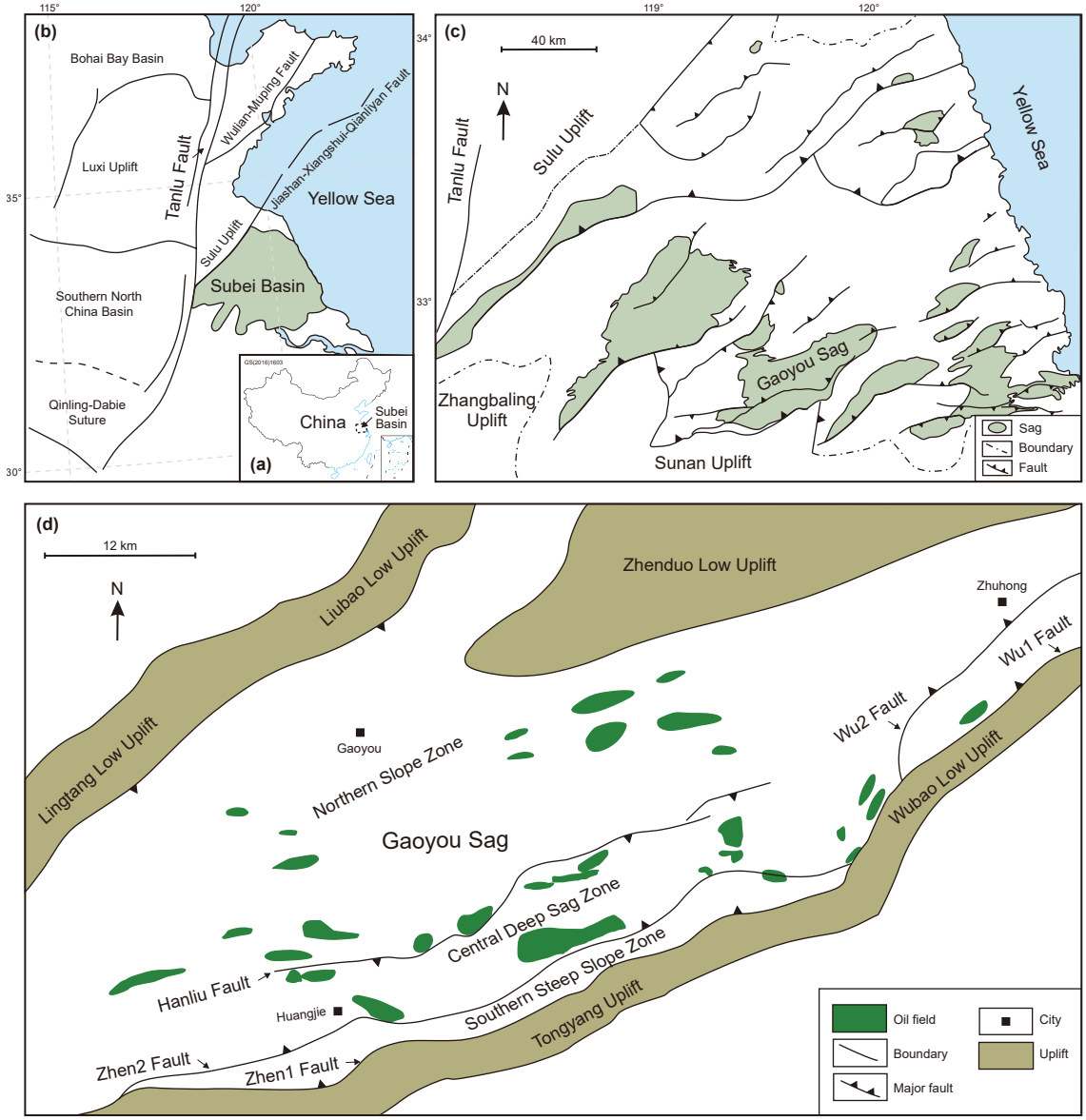

Fig. 1. (**a**–**b**) Geographical location of the Subei Basin in China. (**c**) Distribution of the main tectonic units in the Subei Basin. (**d**) Tectonic outline map of the Gaoyou Sag. Modified from Su et al., (2022).

2.2. Stratigraphy and sedimentology

The Cenozoic stratigraphy of the Gaoyou Sag, from the youngest to the oldest, comprises the Quaternary Dongtai Formation, the Neogene Yancheng Formation, the Eocene Sanduo Formation (E_3s), the Eocene Dainan Formation (E_2d), and the Paleogene Funing Formation (E_1f) (Fig. 2). Among these formations, the first (E_1f_1), second (E_1f_2), and third (E_1f_3) segments of the four-part Funing Formation serve as reservoirs, while the fourth segment (E_1f_4) functions as a hydrocarbon source rock (Quaye et al., 2022).

The Dainan Formation comprises Dainan Member 1 and Dainan Member 2, with thicknesses ranging from 200 to 950 m and 100–900 m, respectively. The primary lithologies include fine sandstone, sandstone, sandy mudstone, and mudstone. On the other hand, the Sanduo Formation consists of Sanduo Member 1 (E_2s_1) and Sanduo Member 2 (E_2s_2), with thicknesses ranging from 100 to 800 m and 50–800 m, respectively (Fig. 2). Its main lithologies include mudstone, muddy sandstone, fine sandstone, and sandy conglomerate. The Dainan Formation primarily represents fluvial, lacustrine, and swamp facies, while the Sanduo Formation reflects deposition in a hilly–fluvial plain terrain, characterized by river floodplains and interfluve basins (Zhu et al., 2023a). During the sedimentation period from E_2d to E_2s_1, two lake transgressions occurred, specifically during the sedimentation period of Dainan Member 1 Sub-member 1 ($E_2d_1^1$) and Sanduo Member 1 Sub-member 6 ($E_2s_1^6$). These events resulted in the formation of shore-shallow lake and semi-deep lake subfacies mudstones, constituting the primary regional cap rocks in the shallow formations of the Gaoyou Sag.

2.3. Cap rock characteristics

2.3.1. Macroscopic characteristics of cap rock

In the Gaoyou Sag, $E_2d_1^1$ comprises five sets of high-conductivity dark mudstones, featuring mud content ranging from 43% to 92%. The western single-layer mudstone exhibits greater thickness, reaching a maximum of around 100 m, while the eastern single-layer mudstone has a maximum thickness of less than 40 m (Fig. 3(a)). Overall, it shows a distribution pattern with thicker layers in the west and thinner layers in the east on the plane. In the Sag, $E_2s_1^6$ comprises one set of high-conductivity dark mudstones characterized by relatively thin mudstone layers. The total thickness is approximately 12–50 m, with the maximum thickness of a single layer reaching up to 12 m (Fig. 3(b)). The mud content ranges from 15% to 56%. The research results indicate that the displacement pressure of the $E_2d_1^1$ cap rock is generally greater

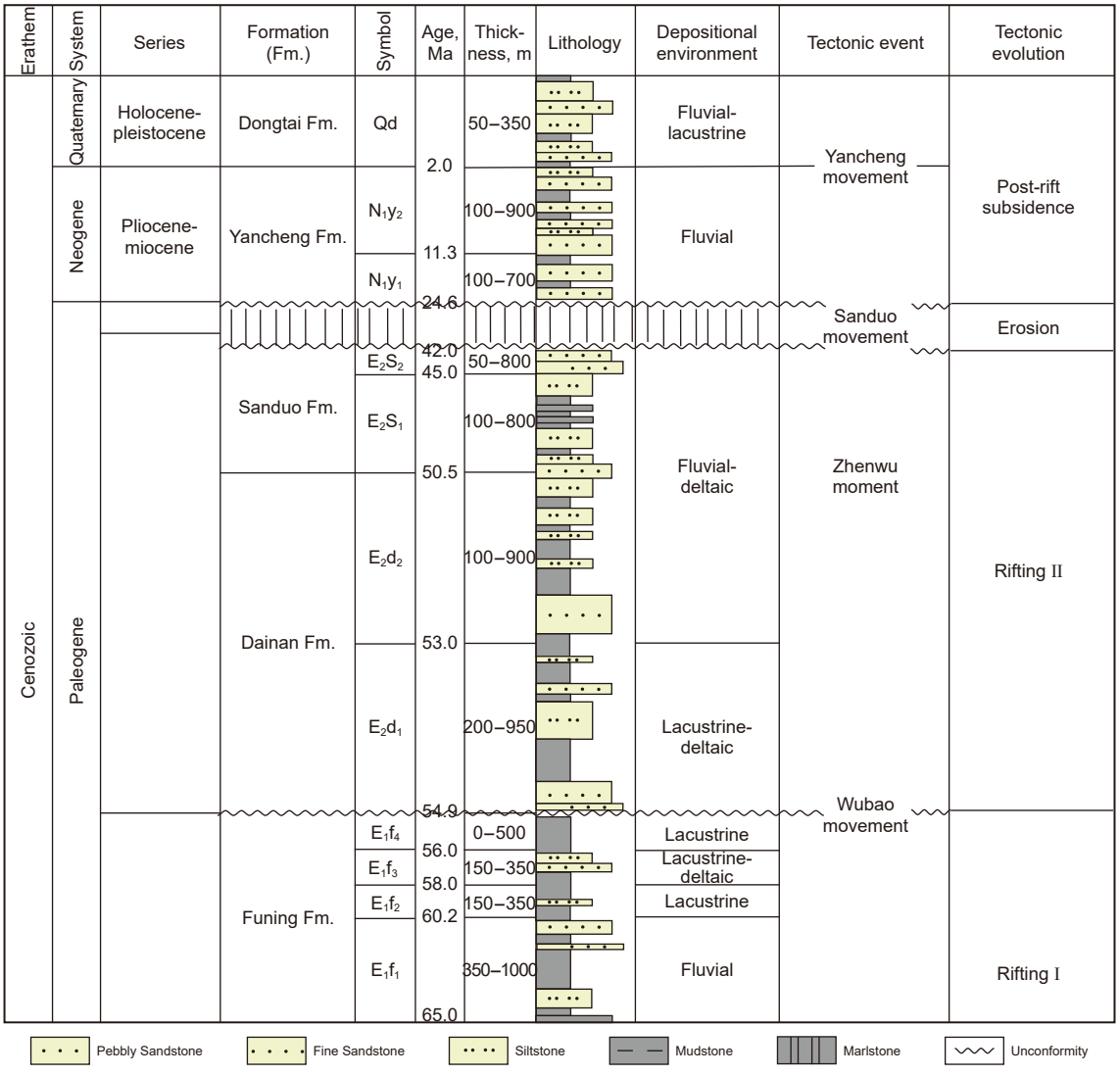

Fig. 2. Stratigraphic column of the Gaoyou Sag in the Subei Basin. Modified from Liu et al., (2017); Su et al., (2022).

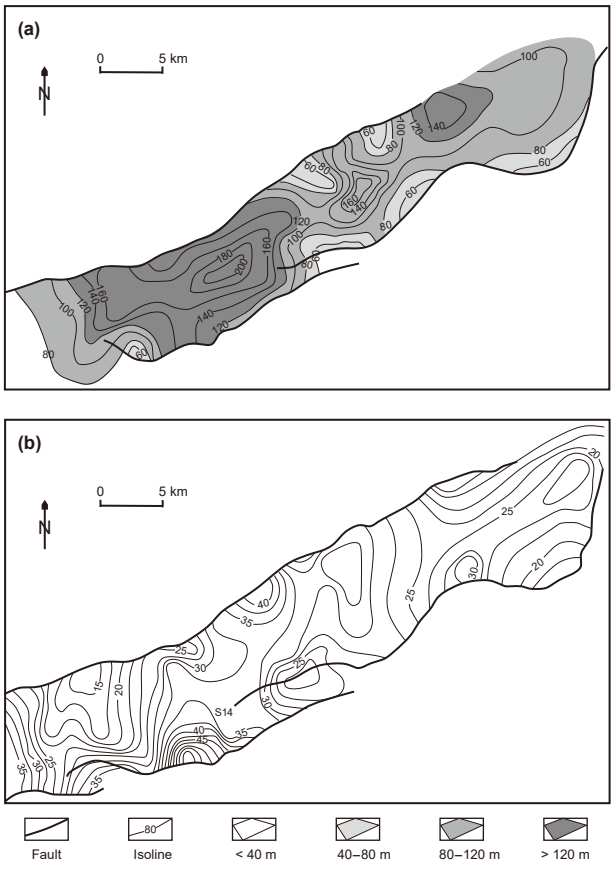

Fig. 3. Mudstone thickness contour map of Gaoyou Sag in Subei Basin, modified from Qiu (2022). (**a**) Mudstone thickness contour map of $E_2d_1^1$. (**b**) Mudstone thickness contour map of $E_2s_1^6$.

than 1 MPa, exceeding 2 MPa in the deep sag zone, with the maximum reaching up to 10 MPa in the central part of the deep Sag. For the $E_2s_1^6$ cap rock, the displacement pressure ranges from 0.5 to 4 MPa, surpassing 2 MPa in the deep sag zone, while in other areas, the displacement pressure is relatively lower, ranging between 1 and 2 MPa (Qiu, 2022).

2.3.2. Microscopic characteristics of cap rock

The results of X-ray diffraction mineralogical analysis for cap rock mudstone samples indicate that illite is the dominant mineral, with an average content of approximately 33.1%, followed by quartz with an average content of about 31.0% (Table 1). The average contents of plagioclase and calcite are 15.5% and 10.5%, respectively. The average content of other minerals, including chlorite, potassium feldspar, and hematite, is less than 5%. The analysis of porosity and permeability for cap rock mudstone samples in the study area reveals that the matrix porosity of the mudstone ranges from 6.67% to 8.62%, with an average value of around 7.85%. The permeability of the overburden matrix is generally less than 0.03 mD, with a minimum value of only 0.001 mD. Overall, the mudstone cap rock in the study area has good sealing properties and can effectively block the leakage of CO_2.

3. Materials and methods

3.1. Materials for fracture research

We collected core data and scanning electron microscope (SEM) images from nine wells, along with triaxial compression test data from four wells in the study area, to analyze natural fractures in the cap rock. Parameters such as fracture dip, density, fillability, and length were examined. Additionally, 18 core samples were analyzed for fracture orientation and permeability. At the same time, basic cap rock data, including physical properties and mineral composition, were compiled to characterize its microscopic features. These data were obtained from the Petroleum Exploration and Development Research Institute, SINOPEC. The investigated samples and applied measurements are shown in Table 2.

3.2. Cap rock natural fracture paleomagnetic orientation

In the study area, there is no oriented core or imaging logging data for the cap rock. The orientation of fractures can be determined using paleomagnetic orientation techniques on core samples (Zeng et al., 2010). Iron-bearing minerals in rocks have the ability to record and preserve the direction of the geomagnetic field. Prolonged exposure to the Earth's magnetic field results in rocks acquiring axial dipole magnetic field properties. Using thermal demagnetization methods, it is possible to obtain vectors for natural remanent magnetization, primary remanent magnetization, and secondary remanent magnetization. In the laboratory, establish the *OXYZ* sample-relative coordinate system, where the *X*-axis, projecting onto the stratum, becomes the X_1-axis (Fig. 4). Subsequently, establish the $O_1X_1Y_1Z_1$ layer coordinate system. The angle θ between the *OXY* plane and the $O_1X_1Y_1Z_1$ plane represents the dip angle of the sample in the stratum. After obtaining the components (*X*, *Y*, *Z*) of the remanent magnetization vector in the sample coordinate system, rotate the *X* and *Z* axes clockwise around the Y-axis by an angle θ to obtain the components (X_1, Y_1, Z_1) of the magnetization vector in the layer coordinate system (Fig. 4). The relationship between the two coordinate systems is expressed as:

$$X_1 = X\cos\theta + Z\sin\theta$$

$$Y_1 = Y$$

Table 2
Investigated samples and applied measurements.

Measurements		Sample quantity	
		Number of samples	Number of wells
Cap rock data collection	Physical property	12	5
	XRD	8	4
	SEM	37	9
	Triaxial compression mechanical tests	6	4
	CO_2-H_2O-Rock reaction test	1	1
Fracture characterization	Paleomagnetic orientation	12	7
	Measurement of CO_2 permeability under different stress conditions	6	3

Table 1
The results of X-ray diffraction mineralogical analysis.

Mineralogy	Chlorite	Illite	Quartz	Potash feldspar	Plagioclase	Calcite	Hematite
Content, %	1.4 – 3.2 / 2.2	26.8 – 40.7 / 33.1	21.2 – 35.0 / 31.0	0.9 – 7.8 / 3.9	6.7 – 24.0 / 15.5	8.2 – 15.6 / 10.5	0 – 3.5 / 1.8

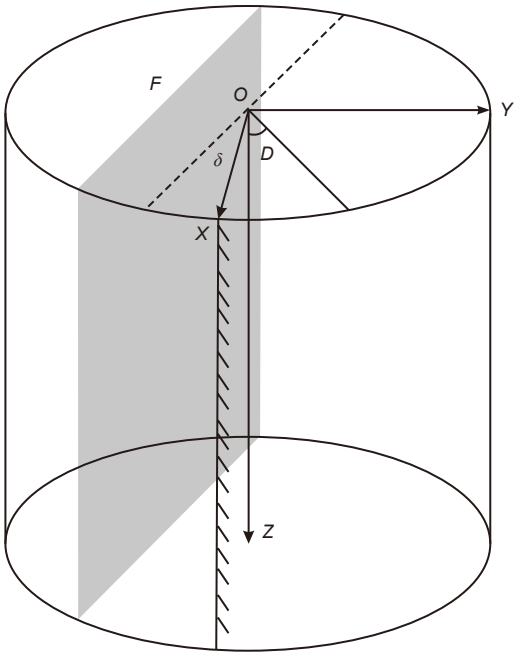

Fig. 4. Schematic diagram of paleomagnetic orientation of fractures. F–fractures; δ–angle between fractures and marker line; D –magnetic declination relative to the marker line.

$$Z_1 = -X \sin\theta + Z \cos\theta$$

Through coordinate transformation, the remanent magnetization vector in natural fractures has been converted to the geographic coordinate system. The above components are transformed into the geographic coordinate system with the X_0-axis oriented to the true north and the Y_0-axis oriented to the east. As the plane coordinate system $O_1X_1Y_1$ and the geographic coordinate system $O_0X_0Y_0$ are in the same plane, therefore:

$$X_0 = X_1 \cos\theta - Y_1 \sin\theta$$

$$Y_0 = X_1 \sin\beta + Y_1 \cos\beta$$

$$Z_0 = Z_1$$

in the formula, β represents the rotation angle around the Z_1 axis.

The current relationship between magnetic declination (D) and magnetic inclination (I) is:

$$\tan D = Y_0/X_0 = \tan[\arctan(Y_1/X_1) + \beta]$$

$$\tan I = Z_0 \Big/ \left(X_0^2 + Y_0^2\right) = Z_1 \Big/ \left(X_1^2 + Y_1^2\right)$$

Therefore, $\beta = D$–arctan(Y_1/X_1), represents the direction of the marker line on the sample in the geographic coordinate system. In the geographic coordinate system, the orientation of the fracture is $\beta + \delta$, where δ is the angle between the fracture on the core and the marker line (Fig. 4).

3.3. Cap rock permeability testing

The experiment was conducted on the GPP-1 high-pressure pore permeability testing system at the State Key Laboratory of Petroleum Resources and Engineering, China University of Petroleum (Beijing) (Fig. 5). Experimental samples were selected from 6 mudstone cores between 1900 and 2200 m in the Paleogene Sanduo Formation and Dainan Formation of the Subei Basin. Permeability characteristic tests for both fractures and matrix were conducted under different stress conditions. Due to the highly fragile and incomplete nature of mudstone core samples containing fractures, testing was challenging. Therefore, artificial fractures were created within the same depth range as natural fractures by splitting to match the inclination angle of natural fractures (Table 3 and Fig. 5). Three core samples were artificially produced to generate fractures with inclinations of 47°, 62°, and 89°, respectively, parallel to the axial direction of the piston sample axis. The stress on the overlying rock mass in the study area is approximately 43–50 MPa, and the final stable confining pressure for the experiment was set at 46 MPa. The experiment followed the calibration method of measuring instruments of core gas (SY/T 6810-2010), a petroleum and natural gas industry standard in China. The experiments were conducted at room temperature (20 °C), using nitrogen gas as the measuring gas, injected along the axial direction of the piston sample at an angle of 90°, and the permeability of the samples was recorded under pressure conditions of 7, 9, 11, 13, 15, 26, 31, 36, 41, and 46 MPa, respectively.

3.4. Cap rock CO_2-H_2O-rock reaction testing

The rock samples used for the CO_2-H_2O-Rock reaction test were obtained from the target section of the cap rock in the Subei Basin. The experimental setup consisted of a high-pressure volumetric pump (0–70 MPa, 0.0001 mL/min), a high-temperature and high-pressure corrosion-resistant reactor (0–150 °C, 0–70 MPa), a BLUE M incubator (0–150 °C), Honeywell pressure sensors, a DBPR-005 back pressure regulator, a measurement system, an iron core support (0–150 °C, 0–70 MPa), and a confining pressure pump (Fig. 6). Initially, the rock cores were cleaned with deionized water,

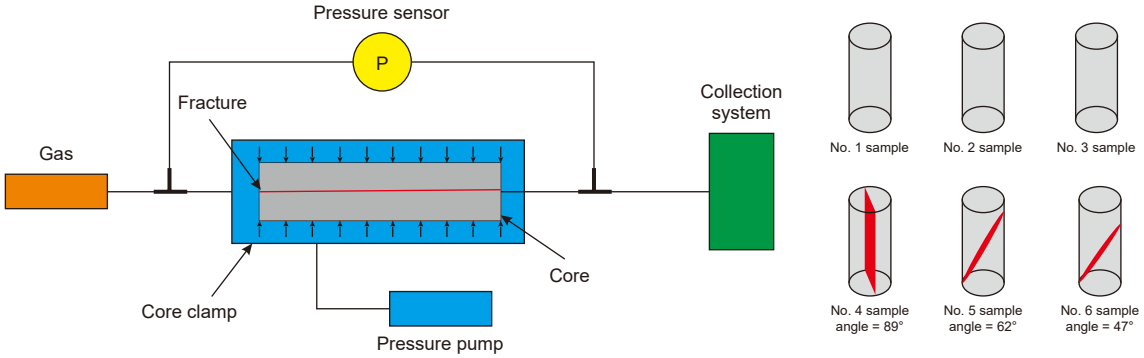

Fig. 5. Schematic diagram of high-pressure pore permeability testing system.

Table 3
Summary of the research materials.

Sample type	No.	Sample size	Lithology	Depth, m	Fracture dip, °	Fracture length, cm
Samples without fractures	1	25mm × 50 mm	Mudstone	1907.3	/	/
	2	25mm × 50 mm	Mudstone	1910.6	/	/
	3	25mm × 50 mm	Mudstone	2000.5	/	/
Samples with fractures	4	25mm × 50 mm	Mudstone	1907.4	89	4.99
	5	25mm × 50 mm	Mudstone	1910.5	62	4.41
	6	25mm × 50 mm	Mudstone	2000.2	47	3.65

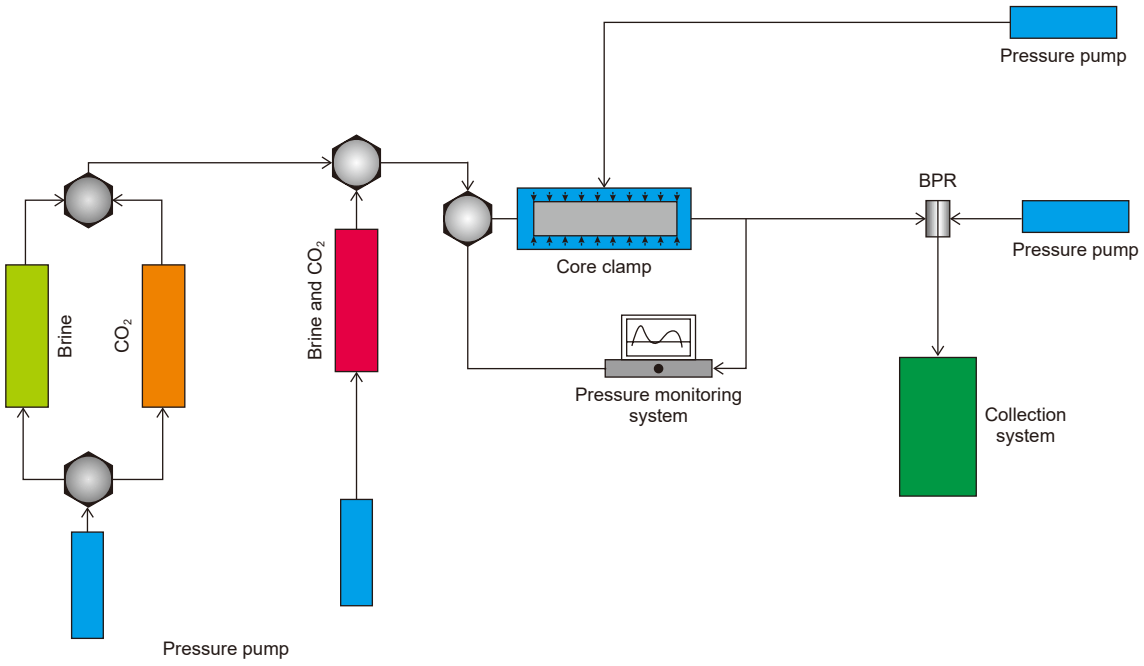

Fig. 6. Schematic diagram of the CO_2-H_2O-Rock reaction device.

dried in a drum, and then the length, diameter, and mass of the cores were measured (Table 4). Brine was prepared and added to the reactor, and the temperature and pressure were adjusted (Chen et al., 2023b). After sufficient reaction, the saturated carbonate solution was displaced, and the gas and water samples generated at different times were recorded. Samples from different reaction times were retrieved, and wet and dry samples were weighed. Mineral types and contents of samples at different reaction times were identified through EDS analysis.

4. Results

4.1. Fracture study

4.1.1. Types and characteristics of fractures

Based on the observation results from core and thin-section data, from the geological origin perspective of natural fractures, the cap rock natural fractures of the Paleogene Sanduo Formation and Dainan Formation in the Gaoyou Sag of the Subei Basin are classified into tectonic fractures and non-tectonic fractures (Figs. 7 and 8).

Tectonic fractures are the main type of natural fractures in the Paleogene Sanduo Formation and Dainan Formation cap rocks in the Gaoyou Sag of the Subei Basin. They are fractures formed under the influence of local tectonic events or tectonic stress fields. Tectonic fractures in the study area include tectonic shear fractures and tectonic slip fractures. Tectonic shear fractures have stable orientations, with straight and smooth surfaces, often showing slickenlines or even stepovers, and sometimes exhibiting calcite mineral fillings (Figs. 7(a), (d), and 8(a)). Tectonic slip fractures are a specific type of low-angle shear fractures that form when shear occurs along weak mudstone layers under tectonic compression or extension. Consequently, the angles between slip fractures and the maximum principal compressive stress (σ_1) do not conform to the shear angle distribution typically described by rock shear fracture criteria (Zeng et al., 2007). These fractures have smooth surfaces, sometimes displaying mirror-like features, with lower dip angles and shorter extension lengths (Fig. 7(b)).

Non-tectonic fractures are mainly composed of diagenetic fractures. Diagenetic fractures result from volume reduction during rock diagenesis, driven by geological processes such as compaction and pressure solution. In the study area, these

Table 4
Summary of the mudstone sample.

No.	Depth, m	Mass, g	Length, cm	Diameter, cm	Quartz, %	Potash feldspar, %	Plagioclase, %	Calcite, %	Chlorite, %	Illite, %
7	1915.7	39.57	3.72	2.50	34.2	4.2	21.3	13.7	1.7	24.9

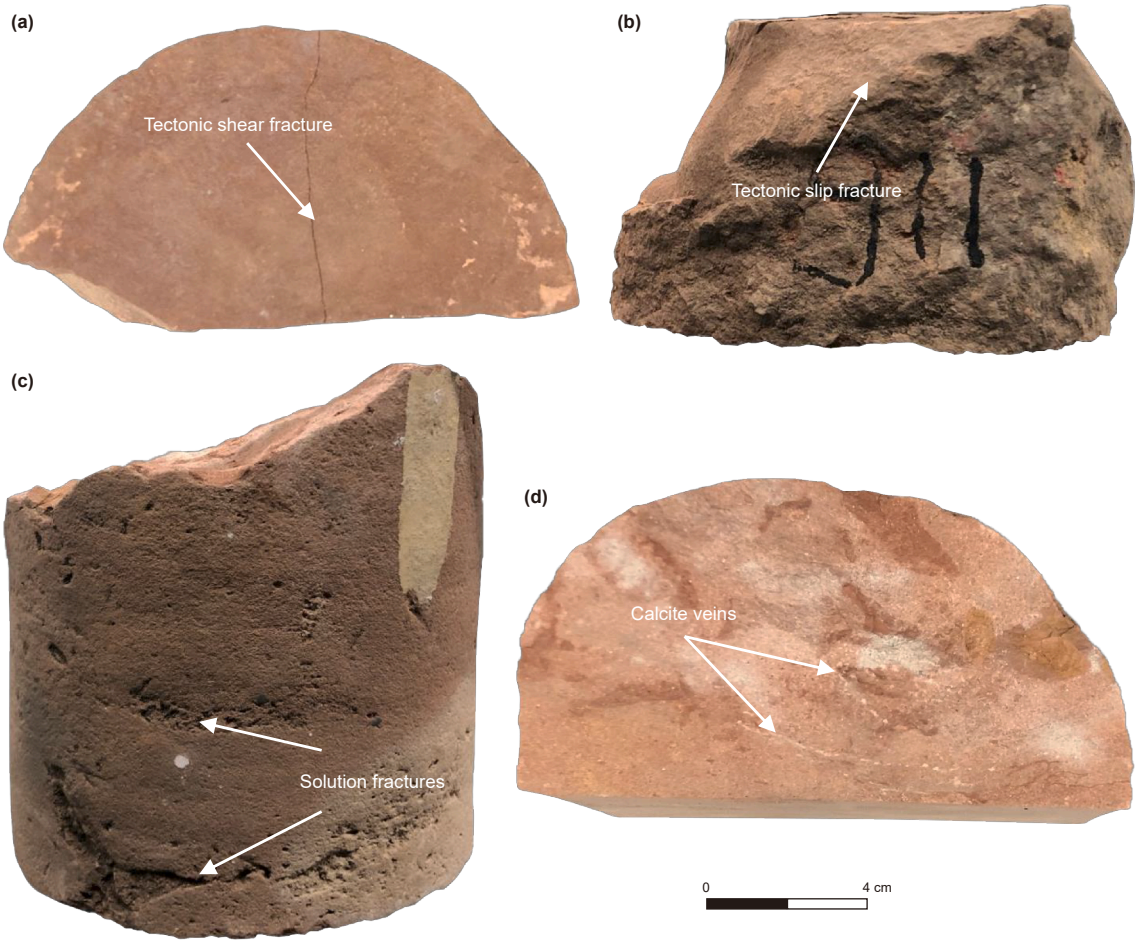

Fig. 7. Core photographs of cap rock fractures. (**a**) High-angle tectonic shear fracture, mudstone, 2027.6 m, Well F51. (**b**) Tectonic slide fracture, mudstone, 1911.3 m, Well F46. (**c**) Dissolution fracture, mudstone, 1949.9 m, Well F38. (**d**) Calcite vein in high-angle tectonic fracture, mudstone, 1920.3 m, Well F44.

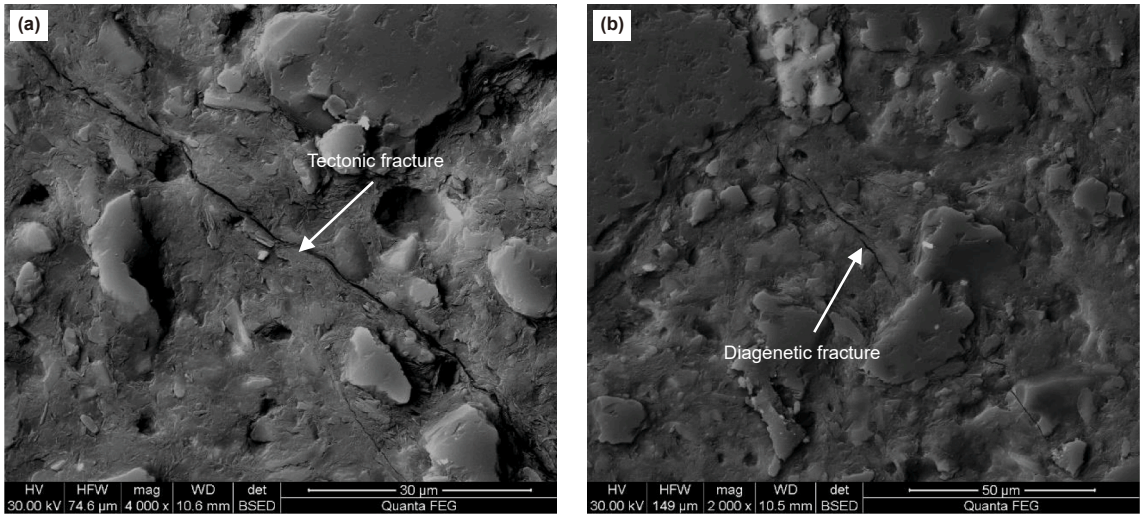

Fig. 8. Scanning electron microscope (SEM) images of cap rock fractures. (**a**) Tectonic fracture, 1997.3 m, Well F12. (**b**) Bedding fracture, 1915.3 m, Well F22.

fractures predominantly manifest as bedding fractures and dissolution fractures. Bedding fractures typically align parallel to the bedding planes, featuring small dip angles and exhibiting characteristics like bending, discontinuity, branching, and termination (Fig. 8(b)). However, they often demonstrate poor continuity. Dissolution fractures originate from differential dissolution processes. They may initially form as fractures and subsequently evolve into bead-like structures through dissolution (Fig. 7(c)). Alternatively, they can arise from the partial or complete dissolution of filling materials. Common features include dissolution pores dispersed around the fractures, and their orientations tend to be unstable.

4.1.2. Fracture occurrence

The results of cap rock fracture orientations determined by core magnetic orientation indicate the presence of four sets of tectonic fractures in the study area, oriented NNW-SSE, NWW-SEE, nearly E-W, and NE-SW (Fig. 9). Among them, NE-oriented tectonic fractures have the highest proportion, followed by NNW-oriented fractures, while nearly E-W and NWW-oriented tectonic fractures have the lowest proportion.

Based on the inclination angle of tectonic fractures, they are classified into nearly vertical fractures (>80°), high-angle fractures (60–80°), intermediate-angle fractures (30–60°), low-angle fractures (10–30°), and nearly horizontal fractures (<10°). The statistical results of fracture dip angles from the core data show that the dip angles of tectonic shear fractures in the study area range between 60° and 90°, predominantly high-angle fractures, with an average dip angle of approximately 82° (Fig. 10). The dip angles of tectonic slip fractures range from 32° to 50°, mainly intermediate-angle fractures, with an average dip angle of around 36° (Fig. 10). Although we did not observe bedding fractures in the core, the dip angles of bedding fractures are expected to be in the range of 0–10°, mainly nearly horizontal fractures.

4.1.3. Fracture length

The statistical results from core drilling indicate that the lengths of tectonic shear fractures in the cap rock of the study area are typically less than 20 cm, mainly distributed in the range of 4–12 cm, with an average fracture length of approximately 7.5 cm (Fig. 11). The scale of tectonic slip fractures is usually less than 10 cm, distributed in the range of 3–6 cm, with an average fracture length of about 3.9 cm (Fig. 11). Thin-section observations show that the lengths of microscopic tectonic fractures range from 100 to 275 μm, with an average length of 160 μm. At the microscopic scale, the lengths of bedding fractures range from 50 to 120 μm, with an average length of 82 μm. Therefore, the lengths of tectonic fractures are greater than those of bedding fractures.

4.1.4. Fracture density

Based on the observation results of core samples in the study area, the linear density of tectonic shear fractures is 0.03 m^{-1}, the linear density of tectonic slip fractures is 0.07 m^{-1}, and the linear density of dissolution fractures is 0.01 m^{-1}. The results indicate differences in linear density among different types of fractures, reflecting variations in the development of different types of fractures.

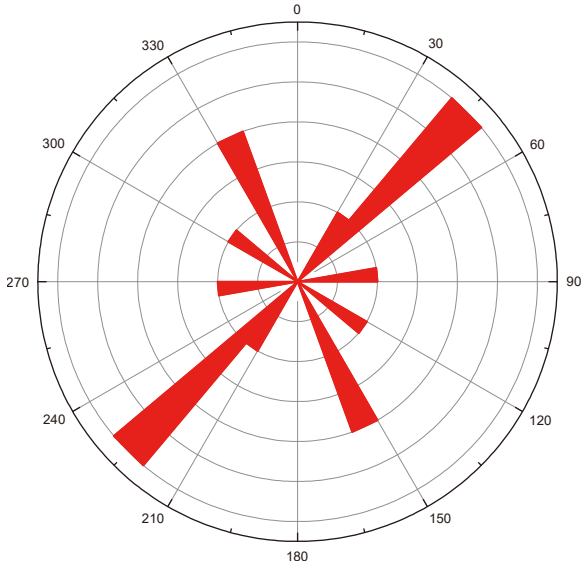

Fig. 9. Rose diagram of cap rock fracture orientations determined by core magnetic orientation ($N = 12$).

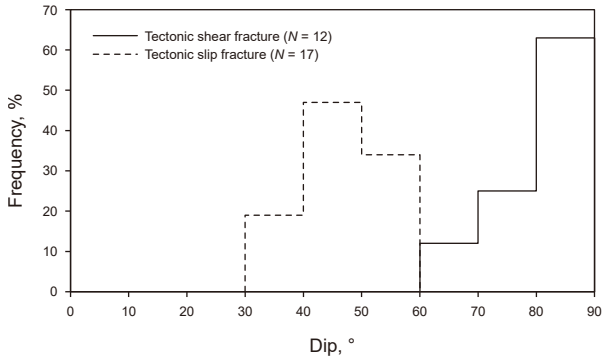

Fig. 10. Histogram of the frequency distribution of cap rock fracture dip angles.

4.1.5. Fracture effectiveness

The evaluation of fracture effectiveness includes the filling characteristics and aperture of the fractures. Based on measurements and observations of core fractures, the effectiveness characteristics of different types of fractures in the cap rock of the study area were determined. The statistical results show that unfilled fractures dominate in tectonic shear fractures, accounting for approximately 85.78%, while fully filled fractures constitute 14.22%, and partially filled fractures were not observed (Fig. 12). The filling material in these fractures is predominantly calcite (Fig. 7(d)). Tectonic slip fractures, bedding fractures, and dissolution fractures are all unfilled, with no observed filling material. The maximum aperture of dissolution fractures is up to 5 mm, with an average of approximately 1.49 mm. The aperture of unfilled tectonic shear fractures, slip fractures, and bedding fractures is generally <100 μm, with an average aperture of approximately 17.29 μm for tectonic shear fractures, 9.45 μm for slip fractures, and the smallest aperture for bedding fractures, averaging about 4.38 μm.

4.2. The opening pressure of cap rock fractures

During the CO_2 injection process, as the pressure increases, fractures in the cap rock open when the pressure surpasses the opening pressure of natural fractures. In this study, the opening pressure of some natural fractures in the cap rock was calculated

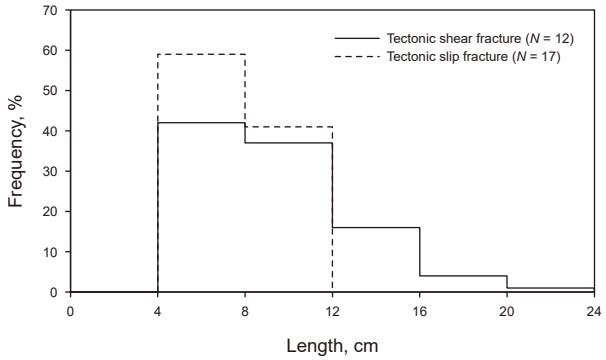

Fig. 11. Histogram of the frequency distribution of cap rock fracture lengths.

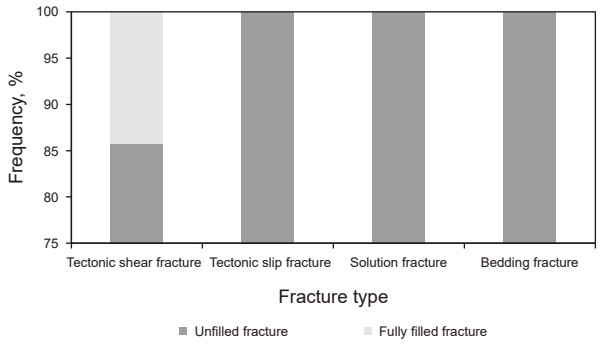

Fig. 12. Statistical results of the filling degree of cap rock fractures ($N = 32$).

as an example. The calculation formula is as follows (Zeng et al., 2008):

$$P_i = \left(\frac{\mu}{1-\mu} H\rho_s g \sin\theta + H\rho_s g \cos\theta - \alpha H\rho_w g\right) \times 10^{-6} \pm Hf\sigma_1 \sin\beta\cos\beta \pm Hf\sigma_3 \sin\beta\cos\beta$$

in the equation, P_i represents the static closure pressure of natural fractures, MPa; μ is the Poisson's ratio of the rock, dimensionless; α is the formation pressure coefficient, dimensionless; H is the burial depth of the fracture, m; θ is the dip angle of the fracture, °; ρ_s is the rock density, kg/m^3; ρ_w is the density of water, kg/m^3; g is the gravitational acceleration, N/kg; β is the angle between the current horizontal maximum principal stress and the fracture trend, °; $f\sigma_1$ and $f\sigma_3$ are the gradients of the horizontal maximum and minimum principal stresses, with positive values indicating compressive stress and negative values indicating tensile stress, MPa/m. The Poisson's ratio (μ) is determined through rock mechanics experiments. The study area exhibits normal formation pressure, with the pressure coefficient ranging from 0.8 to 1.0; α is considered as the average value, 0.9; ρ_s, ρ_w, H, and θ are all based on measured data; the current direction of the maximum horizontal principal stress is approximately E-W, and the fracture trend is determined by core magnetic orientation to obtain β; the current maximum principal stress gradient is approximately −0.01509 MPa/m, and the minimum principal stress gradient is 0.0196 MPa/m (Chen, 2009). The calculation results are shown in Table 5.

4.3. The permeability of cap rock fractures

The experimental results of overburden gas permeability for samples without fractures show that, with increasing confining pressure, the matrix permeability of samples at different burial depths gradually decreases (Fig. 13). When the confining pressure is less than 9 MPa, the matrix permeability declines rapidly, with shallower samples exhibiting a significantly greater reduction compared to the sample at a burial depth of 2000.5 m. As the confining pressure increases to between 9 and 13 MPa, the rate of permeability reduction gradually slows down. With a further increase in confining pressure beyond 13 MPa, the matrix permeability of samples at different burial depths becomes nearly identical, decreasing to approximately 0.00015 mD. Thereafter, as the pressure continues to rise, the matrix permeability gradually stabilizes at around 0.00003 mD.

The results of permeability tests on samples containing fractures indicate that their permeability is higher by 3–4 orders of magnitude compared to samples without fractures (Fig. 14). Therefore, it is considered that the permeability of samples containing fractures is approximately equal to the permeability of the fractures within the samples. Experimental results show that with increasing pressure, the permeability of fractures exhibits a more pronounced power-law decay, eventually stabilizing. Even when the confining pressure reaches 46 MPa, the permeability of fractures can still exceed 10 mD, indicating that cap rock fractures have a strong permeability to CO_2. Furthermore, with increasing confining pressure, samples with fractures of different dip angles exhibit significant differences in permeability characteristics. On one hand, the smaller the dip angle of the fractures, the lower the permeability of the samples under maximum confining pressure conditions. On the other hand, fractures with different dip angles show variations in sensitivity to pressure; as pressure increases, samples with larger dip angles experience a significantly higher rate of permeability reduction compared to samples with smaller dip angles. Additionally, core observations confirm a significant difference in the dip angle distribution between tectonic shear fractures and tectonic slip fractures. The former is mainly distributed between 60 and 90°, while the latter ranges between 32 and 50°. Therefore, compared to tectonic slip fractures, tectonic shear fractures exhibit greater stress sensitivity.

4.4. Cap rock CO_2-H_2O-rock reaction

The results of changes in the content of various mineral components with CO_2 sequestration time indicate that quartz, with SiO_2 as its main component, exhibits stable properties. The quartz content increased from 34.2% to 37.1%. A comparison of data at different times reveals a slight increase in quartz content (Fig. 15).

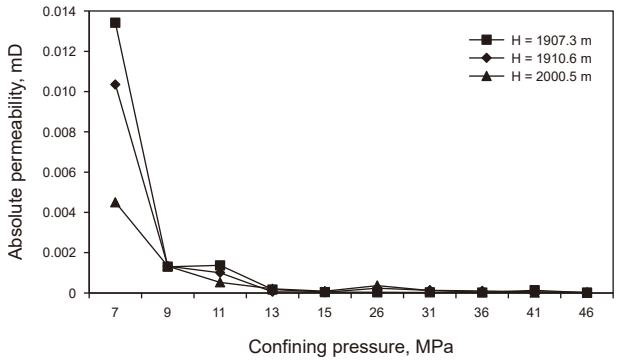

Fig. 13. Permeability-pressure relationship diagram of core samples without fractures.

Table 5
Calculation results of opening pressure for cap rock fractures.

Sample No.	H, m	Fracture strike	θ, °	μ	ρ_s, kg/m^3	ρ_w, kg/m^3	$f\sigma_1$, MPa/m	$f\sigma_3$, MPa/m	β, °	P_i, MPa
8	1907.4	NNW-SSE	89	0.26	2500	1020	−0.01509	0.00025	60	25.23
9	1910.5	NWW-SEE	62	0.38	2610	1020	−0.01509	0.00025	30	45.29
10	2000.2	NE-SW	47	0.41	2430	1020	−0.01509	0.00025	45	54.57
11	2036.8	E-W	75	0.38	2500	1020	−0.01509	0.00025	0	24.63
Average value	1963.7	/	68.3	0.36	2510	1020	−0.01509	0.00025	33.8	/

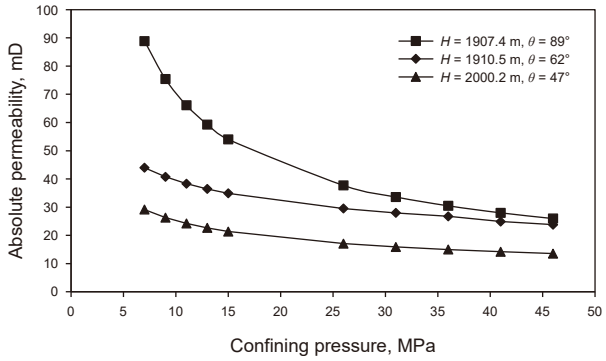

Fig. 14. Permeability-pressure relationship diagram of core samples with fractures.

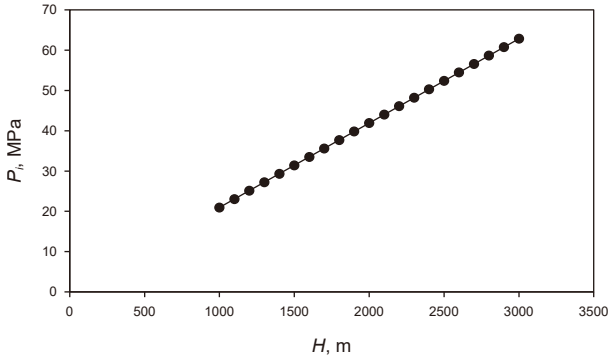

Fig. 16. Relationship between the burial depth of fractures and the opening pressure of fractures when $\theta = 68.3°$ and $\beta = 33.8°$. The average value of μ for 4 samples is taken as 0.36, and the average value of ρ_s for 4 samples is 2510 kg/m^3.

Potassium feldspar, mainly composed of $KAlSi_3O_8$, saw its content rise from 4.2% to 10.7% (Fig. 15). Plagioclase, composed primarily of $NaAlSi_3O_8$, experienced an increase in content from 21.3% to 31.7% (Fig. 15). Calcite, mainly consisting of $CaCO_3$, initially decreased in content from 10.7% to 1.4%, then increased to 7%, before decreasing to 0 (Fig. 15). Clay minerals, primarily composed of kaolinite, illite, and montmorillonite, decreased overall from 29.6% to 20.5% (Fig. 15). Dolomite, composed mainly of $CaMg(CO_3)_2$, increased from 0 to 8.2%, then decreased back to 0 (Fig. 15).

5. Discussion

5.1. Factors influencing the opening pressure of cap rock fractures and their impact on CO_2 geological storage

5.1.1. Factors influencing the opening pressure of cap rock fractures

(1) Fracture burial depth

Due to the influence of the current stress field, fractures with different orientations at the same depth experience varying opening pressures. Therefore, when studying the impact of fracture burial depth on the opening pressure, it is necessary to focus on fractures with the same orientation. Under the same orientation conditions (fracture dip angle (θ) = 68.3°, fracture dip angle between the current horizontal maximum principal stress and the fracture trend (β) = 33.8°), the relationship between burial depth (H) and opening pressure (P_i) indicates that for fractures with the same orientation and dip angle, the deeper the burial position, the greater the opening pressure, making it more difficult for the fractures to open (Fig. 16). These two factors show a positive correlation. This is because, as the depth of fracture burial increases, the overlying confining pressure acting on the fracture surface increases. Consequently, the pressure required for the fracture to reopen becomes greater, resulting in a larger opening pressure for underground fractures. Therefore, considering the similar development characteristics of cap rock fractures in the Sanduo Formation and Dainan Formation in the study area, the Dainan Formation, with its deeper burial depth than the Sanduo Formation, requires a greater opening pressure for fractures to open. Consequently, the cap rock of the Dainan Formation is more effective for the CO_2 geological storage.

(2) Fracture orientation and current stress

The relationship between different β and θ values and P_i indicates that within the same depth range, fractures with dip angles distributed between 45° and 90°, sharing the same trend, have smaller opening pressures for larger dip angles, making them more prone to opening (Fig. 17). Fractures with dip angles distributed between 0° and 45°, sharing the same trend, have smaller opening pressures for smaller dip angles, making them more prone to opening (Fig. 18). Additionally, among fractures with the same dip angle, those with smaller angles between their trend and the current maximum horizontal principal stress have

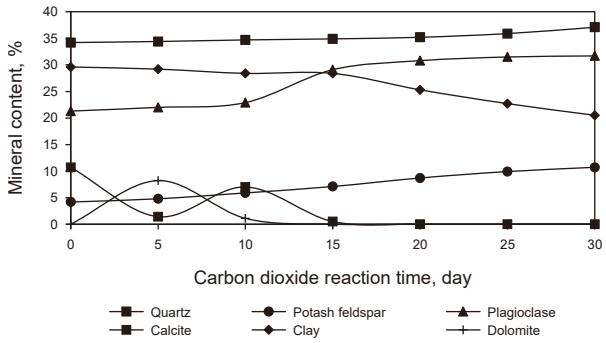

Fig. 15. Relationship between the change in rock mineral composition and the reaction time with CO_2.

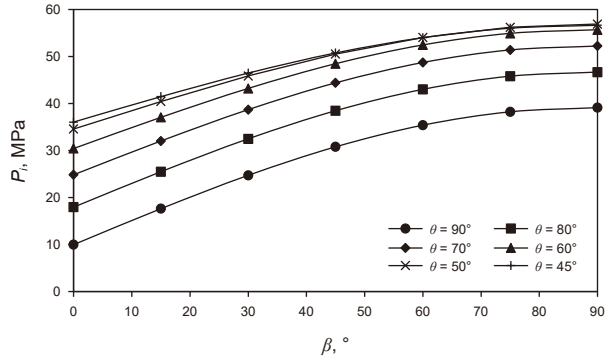

Fig. 17. Relationship between the angle between the current maximum horizontal principal stress direction and the fracture trend and the opening pressure of fractures (θ = 45–90°). H is the average value taken from 4 samples, 1963.7 m; μ is the average value taken from 4 samples, 0.36; ρ_s is the average value taken from 4 samples, 2510 kg/m^3.

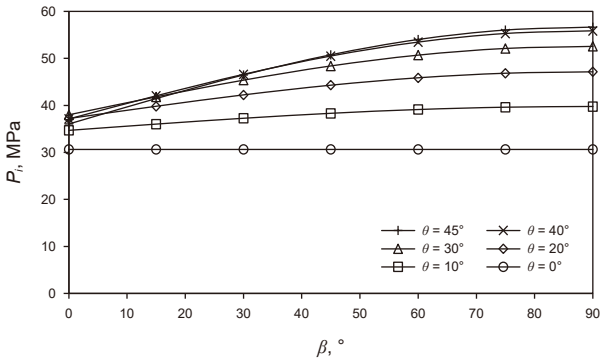

Fig. 18. Relationship between the angle between the current maximum horizontal principal stress direction and the fracture trend and the opening pressure of fractures ($\theta = 0$–$45°$). H is the average value taken from 4 samples, 1963.7 m; μ is the average value taken from 4 samples, 0.36; ρ_s is the average value taken from 4 samples, 2510 kg/m^3.

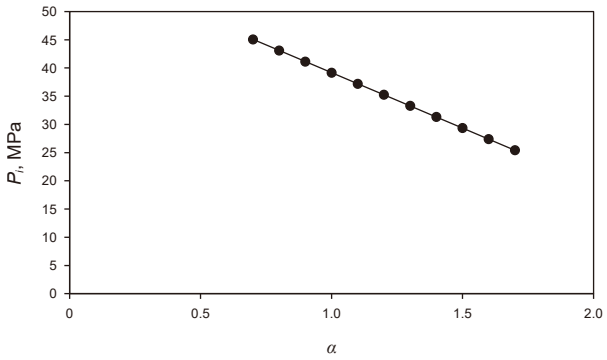

Fig. 19. Relationship between the coefficient of formation pressure and the opening pressure of fractures at $\theta = 68.3°$, $\beta = 33.8°$, $H = 1963.7$ m. μ is the average value taken from 4 samples, 0.36; ρ_s is the average value taken from 4 samples, 2510 kg/m^3.

smaller opening pressures, making them more prone to opening (Figs. 17 and 18). The influence of the current stress field on the opening pressure of fractures is mainly manifested when, under constant conditions, the smaller the angle between the direction of the maximum principal stress and the trend of the fracture, the smaller the opening pressure of the fracture. Conversely, the larger the angle, the greater the opening pressure of the fracture. As the orientation of fractures changes, the static rock confining pressure experienced by the fracture surfaces varies, leading to different pressures required for the fractures to reopen. Fractures nearly parallel to the direction of the maximum principal stress ($\beta = 0°$) are in a tensile state with a large underground opening, resulting in the minimum opening pressure. Fractures nearly perpendicular to the direction of the maximum principal stress ($\beta = 90°$) are in a compressive state with a small underground opening, resulting in the maximum opening pressure. Fractures obliquely intersecting with the direction of the maximum principal stress exhibit a combined tensile and shear state with an underground opening between the aforementioned two cases, resulting in an opening pressure between the two extremes. It is worth noting that when the dip angle of fractures is distributed between 0° and 10°, the angle between the current stress field direction and the trend of the fracture has almost no effect on the opening pressure of the fracture. At this point, the opening pressure of the fracture is only influenced by the overlying formation pressure. Based on the development characteristics of natural fractures in the study area, the opening pressure of fractures with different orientations, arranged from smallest to largest, is approximately as follows: nearly E-W, NWW-SEE, NE-SW, and NNW-SSE directions.

(3) Pore fluid pressure

The relationship between the formation pressure coefficient and the opening pressure of fractures indicates that, within the same depth range, fractures with the same orientation in an abnormally high-pressure fluid environment have smaller opening pressures compared to fractures in a static hydrostatic pressure environment (Fig. 19). Fractures in an abnormally high-pressure environment are more easily opened because the fluid bears a greater load, reducing the confining pressure effect on the fractures, i.e., decreasing the opening pressure of the fractures. Conversely, when the pore fluid pressure is less than static hydrostatic pressure, the skeleton bears more force, leading to an increase in the opening pressure of the fractures. Therefore, cap rocks in low-pressure or ambient-pressure environments are less prone to fracture opening compared to those in high-pressure environments, exhibiting better CO_2 storage capacity.

5.1.2. The impact of opening pressure of cap rock fractures on CO_2 geological storage

With the increasing injection of CO_2, the formation pressure gradually rises, causing instability in the formation. The range affected by pressure increments in the cap rock continues to expand (Qin et al., 2022). If the pressure within the cap rock becomes too high, it not only leads to the formation of new fractures but also results in the further opening, extension, and expansion of existing natural fractures in the cap rock, leading to the failure of CO_2 storage (Lavrov, 2016). Due to the generally lower opening pressure of existing natural fractures, especially high-angle tectonic fractures, compared to the formation fracturing pressure, the injection pressure may cause fractures to open and extend before inducing formation fracturing (Zeng et al., 2023). In this scenario, determining reasonable CO_2 injection pressure limits should not rely on the formation fracturing pressure but rather on the opening pressure of fractures to avoid widespread fracture opening and CO_2 leakage. For CO_2 geological storage, critical input parameters such as the shallowest burial depth of the cap rock, the maximum value of the formation pressure coefficient, the maximum dip angle of fractures, and the minimum angle between the current maximum principal stress direction and fracture trend should be chosen. This approach will help control internal pressure within the cap rock, prevent further opening and extension of cap rock fractures, and effectively enhance the overall CO_2 storage capacity.

5.2. Factors influencing the permeability of cap rock fractures and their impact on CO_2 geological storage

5.2.1. Factors influencing the permeability of cap rock fractures

(1) Fracture orientation and current maximum principal stress

Under the influence of overlying lithostatic pressure, the normal stress acting on the low-angle fracture surface is significantly greater than that on the high-angle fracture surface. This

results in larger apertures for high-angle fractures compared to low-angle fractures, indicating better effectiveness. Therefore, as the dip angle of fractures increases, the permeability of fractures also increases. The relationship between the fracture trend and the direction of the current maximum principal stress is as follows: fractures parallel to the current maximum principal stress direction have larger apertures, better connectivity, higher permeability, and represent the main flow direction. In contrast, fractures perpendicular to the current maximum principal stress direction, due to the larger normal stress acting perpendicular to the fracture surface, tend to be closed and are less effective. Fractures with orientations oblique to the current maximum principal stress direction fall between the two categories, and as the angle between them increases, the aperture and permeability of fractures decrease (Zeng and Li, 2009). Therefore, fractures with larger dip angles and orientations consistent with the current stress direction exhibit the highest permeability.

(2) Effective stress

External effective stress is a crucial factor influencing the permeability of cap rock fractures, and fractures with different dip angles exhibit significant pressure sensitivity. Under the influence of overlying lithostatic pressure, the normal stress acting on the low-angle fracture surface is notably greater than that on the high-angle fracture surface. Consequently, high-angle fractures exhibit larger apertures than low-angle fractures, indicating a stronger permeability for high-angle fractures. Therefore, as the dip angle of fractures decreases and effective stress increases, the aperture of fractures decreases, leading to a reduction in the permeability of fractures. It is worth noting that, despite the decrease in aperture, experimental results on fracture permeability indicate that in the deep Jurassic tight sandstone reservoirs at the southern margin of the Junggar Basin, where fracture burial depth exceeds 8000 m (with confining and axial pressures reaching 115 MPa), the fracture permeability can still reach around 20 mD (Mao et al., 2020). The permeability of natural fractures remains over 400 times higher than the matrix permeability of the reservoir. Therefore, natural fractures continue to serve as essential storage spaces and main flow channels in deep tight reservoirs. It can be reasonably inferred that natural fractures in the cap rock may not completely close with increasing effective stress or burial depth. Natural fractures remain potential pathways for CO_2 leakage, posing an increased risk of CO_2 storage failure.

(3) Mineral composition of fractures and types of fillings

Based on the filling conditions of natural fractures, they can be classified as unfilled, partially filled, or fully filled (Zhang et al., 2021b). Unfilled fractures consist of the fracture walls and voids, partially filled fractures consist of the fracture walls, voids, and filling materials, while filled fractures consist of the fracture walls and filling materials. In the study area, cap rock fractures were found to be filled only with calcite, and other common types of natural fracture fillings include minerals like quartz, clay, and dolomite (Zeng et al., 2012). The fracture walls may be composed of carbonate or silicate minerals. Under the influence of carbonation, fracture walls or filling materials may undergo dissolution or form new mineral precipitates, leading to changes in fracture aperture or closure and alterations in fracture permeability (Laubach et al., 2019; Laubach, 2003). Therefore, it is essential to consider the mineral composition of fracture walls and the types of filling materials.

In acidic environments, most silicate minerals, including feldspar, mica, and clay minerals, exhibit high instability and are prone to dissolution in water (Fig. 15). Simultaneously, under suitable conditions, new minerals can form (Pham et al., 2011; Zhang et al., 2015). As the H^+ concentration increases, the dissolution rates of most silicate minerals rapidly increase exponentially, while the dissolution rate of quartz remains nearly constant or even slowly decreases (Dove and Crerar, 1990). Consequently, for unfilled fractures with quartz as the component of the fracture walls, there is minimal reaction with carbonic acid, resulting in little to no change in the aperture and permeability of the fractures. However, if the mineral composition of the fracture walls includes other silicate minerals, new mineral precipitates may form. For instance, minerals such as kaolinite, muscovite, alunite, and quartz could potentially obstruct the fracture pathways, reducing the permeability of the fractures (Rosenbauer et al., 2005; Watson et al., 2004). Similarly, if the filling material in the fractures is clay minerals, especially smectite, it may react with H_2CO_3 to form new minerals such as iron dolomite, quartz, and kaolinite (Kurnosov et al., 2020), resulting in minimal changes in the permeability of the fractures. Since quartz-filled fractures resist dissolution by H_2CO_3, the permeability of quartz-filled fractures remains almost unchanged. The increased amount of quartz primarily stems from the reaction between H_2CO_3 and smectite and feldspar. Most carbonate minerals, such as calcite, magnesite, siderite, and dolomite, are susceptible to reactions with carbonic acid (Fig. 15). For unfilled fractures with carbonate minerals as components of the fracture walls, they may react with carbonic acid and dissolve (Du et al., 2018; Yu et al., 2012), resulting in localized increases in fracture aperture. Similarly, if the filling material in the fractures comprises calcite and dolomite veins, the veins may gradually dissolve in H_2CO_3, creating localized high-permeability channels and significantly increasing the permeability of the fractures. It is worth noting that when CO_2 is injected into geological formations containing calcite-filled fractures, it can react with the groundwater and existing calcite minerals. This reaction may lead to the dissolution of calcite, releasing calcium and carbonate ions into the solution. Under certain conditions such as changes in pressure, temperature, or chemical composition of the solution, these calcium and carbonate ions may re-precipitate as carbonate minerals, such as calcite or dolomite, within the fractures. Therefore, early exposure to H_2O and CO_2 may result in an increase in the content of calcite and dolomite, but ultimately, they will be completely dissolved (Fig. 15).

5.2.2. Impact of permeability of cap rock fractures on geological storage of CO_2

After the injection of CO_2 into the reservoir, it migrates upward continuously under the influence of buoyancy and injection pressure, accumulating extensively beneath the cap rock. CO_2 infiltrates the cap rock by breaking through capillary forces between the reservoir and cap rock or using fractures between the reservoir and cap rock as pathways. Consequently, CO_2-H_2O-Rock reactions occur within the cap rock fractures. In the context of oil and gas reservoir exploration and development, filled fractures, having nearly lost their permeability, are considered ineffective. Partially filled and unfilled fractures, exhibiting permeability, are deemed effective. Initially, unfilled fractures in the cap rock have higher permeability. As the CO_2-H_2O-Rock reaction progresses, CO_2

encounters silicate minerals in the cap rock fracture pathways, resulting in either new precipitation or no reaction. This leads to a reduction or minimal change in the fractures' permeability to CO_2. In cap rock fractures where CO_2 encounters carbonate minerals, dissolution occurs, increasing the aperture of the fractures and enhancing the permeability to CO_2, consequently raising the risk of CO_2 leakage. Filled fractures in the cap rock initially have lower porosity and permeability, providing minimal conduits for CO_2 migration. As the CO_2-H_2O-Rock reaction continues, the permeability of fractures filled with quartz and clay remains essentially unchanged. The former experiences no CO_2-H_2O-Rock reaction, while the latter forms new mineral precipitates, promoting fracture closure. Fractures filled with calcite and dolomite witness an increase in permeability as the CO_2-H_2O-Rock reaction progresses. After the complete dissolution of the veins, the permeability of fractures is jointly controlled by effective stress, fracture orientation, and the current maximum principal stress. Therefore, changes in CO_2 permeability follow a similar trend to unfilled fractures. Regardless of whether it is carbonate minerals in fracture walls or fracture fillings, in the CO_2-H_2O-Rock system, besides the dissolution of carbonate cement in fractures, variations in CO_2 concentration, pressure, ambient temperature, hydrodynamic conditions, and calcium ion concentration can lead to the formation of carbonate cement (Xu et al., 2003; Zhu et al., 2011). Secondary precipitation processes can result in the plugging of fractures with calcite and dolomite, aiding in self-sealing of the fractures, which may potentially reduce their permeability. Thus, during the geological storage of carbon dioxide, changes in other conditions are also significant factors affecting the CO_2-H_2O-Rock reaction in cap rocks and the permeability of carbonate-filled fractures.

Overall, different types of fractures exhibit varying impacts on CO_2 geological storage. High-angle tectonic fractures and fractures oriented parallel to the current stress direction pose the highest risk of leakage in CO_2 geological storage. In comparison to high-angle tectonic fractures, laterally distributed bedding fractures dominate the lateral migration of CO_2. The intermittent and discontinuous distribution of these bedding fractures, coupled with the influence of overlying formation pressure, results in relatively poor aperture and permeability, thereby reducing the risk of CO_2 leakage into the cap rock. The impact of differently filled fractures on CO_2 geological storage is characterized by a higher risk of CO_2 leakage in fractures filled with carbonate minerals like calcite and dolomite due to prolonged CO_2-H_2O-Rock reactions. In contrast, fractures filled with silicate minerals such as quartz pose a lower risk of CO_2 leakage.

6. Conclusions

(1) In the Gaoyou Sag of the Subei Basin, mudstone cap rocks from the Paleogene Sanduo and Dainan Formations contain tectonic (shear and slip) and non-tectonic (bedding and dissolution) fractures. Tectonic fractures trend NNW-SSE, NWW-SEE, E-W, and NE-SW. Shear fractures are high-angle, slip fractures are moderate-angle, and bedding fractures are near-horizontal. Tectonic fractures are larger but less dense than diagenetic ones, with some fully filled by calcite.

(2) Natural fractures significantly increase CO_2 leakage risk. Fractured samples have permeability three to four orders of magnitude higher than intact samples. Fracture permeability decreases with pressure but remains above 10 mD even at 46 MPa.

(3) CO_2 injection pressure limits should be based on fracture opening pressure rather than cap rock fracturing pressure. Factors like burial depth, fracture dip, and alignment with the maximum principal stress should be considered to prevent further fracture opening and CO_2 leakage.

(4) Fracture permeability is controlled by orientation, stress, mineral composition, and filling material. High-angle fractures aligned with the stress direction have the highest permeability. Increased effective stress reduces permeability, while CO_2-H_2O-Rock interactions modify permeability based on mineral content.

(5) High-angle fractures aligned with the stress direction pose the greatest CO_2 leakage risk. Bedding fractures promote lateral CO_2 migration, reducing vertical leakage risk. Fractures filled with carbonates (calcite, dolomite) are more susceptible to CO_2-H_2O-Rock reactions, while silicate-filled fractures (quartz) present lower risks.

CRediT authorship contribution statement

Yun-Zhao Zhang: Data curation, Conceptualization, Formal analysis. **Quan-Qi Dai:** Funding acquisition, Data curation, Formal analysis. **Lian-Bo Zeng:** Data curation, Formal analysis. **Rui-Qi Li:** Methodology, Investigation. **Rong-Jun Zhang:** Funding acquisition, Investigation. **Le Qu:** Formal analysis, Data curation. **Yang-Wen Zhu:** Funding acquisition, Formal analysis. **Hai-Ying Liao:** Methodology, Project administration. **Hao Wu:** Writing – review & editing, Writing – original draft.

Declaration of competing interest

No conflict of interest exits in the submission of this manuscript, and manuscript is approved by all authors for publication. I would like to declare on behalf of my co-authors that the work described was original research that has not been published previously, and not under consideration for publication elsewhere, in whole or in part. All the authors listed have approved the manuscript that is enclosed.

Acknowledgment

This study was financially supported by the National Natural Science Foundation of China (Grant No. 42402171), the China Postdoctoral Science Foundation (Grant No. 2023MD744255), the Natural Science Basic Research Program of Shaanxi (Grant No. 2024JC-YBQN-0353), the Scientific Research Program Funded by Shaanxi Provincial Education Department (No. 23JK0600), the Shaanxi Postdoctoral Science Foundation (Grant No. 2023B SHEDZZ324), the project of Theory of Hydrocarbon Enrichment under Multi-Spheric Interactions of the Earth (Grant No. THEMSIE04010107), the Key Research and Development Program of Shaanxi (Grant No. 2021KW-10), the Innovation Capability Support Program of Shaanxi (Grant No. 2022PT-08), and the SINOPEC CCUS Fund Project (Grant No. 33550000-22-ZC0613-0326).

CO_2-H_2O-rock interaction equation

$$CO_2 + H_2O \rightleftharpoons H_2CO_3$$

$$2KAlSi_3O_8(\text{Potassium feldspar}) + 2H^+ + 9H_20 = Al_2Si_2O_5(OH)_4\downarrow (\text{Kaolinite}) + 2K^+ + 4H_4SiO_4$$

$$2NaAlSi_3O_8(\text{Albite}) + 3H_20 + 2CO_2 = Al_2Si_2O_5(OH)_4\downarrow(\text{Kaolinite}) + 4SiO_2\downarrow(\text{Quartz}) + 2Na^+ + 2HCO_3^-$$

$$NaAlSi_3O_8(\text{Albite}) + H_20 + CO_2 = NaAlCO_3(OH)_2(\text{Dawsonite}) + 3SiO_2\downarrow(\text{Quartz})$$

$$\left[\frac{Fe}{Mg}\right]_5 Al_2Si_2O_{10}(OH)_8\downarrow(\text{Chlorite}) + 5CaCO_3 + 5CO_2 = 5Ca\left[\frac{Fe}{Mg}\right](CO_3)_2\downarrow(\text{Magnesium} - \text{Iron Dolomite}) + Al_2Si_2O_5(OH)_4\downarrow(\text{Kaolinite}) + SiO_2\downarrow(\text{Quartz}) + 2H_2O$$

$$CO_2 + H_2O + CaCO_3(\text{Calcite}) = Ca(HCO_3)_2$$

$$CO_2 + H_2O + MgCO_3(\text{Magnesite}) = Mg(HCO_3)_2$$

$$CO_2 + H_2O + FeCO_3(\text{Siderite}) = Fe(HCO_3)_2$$

$$CaMg(CO_3)_2(\text{Dolomite}) + 2H_2CO_3 = Ca^{2+} + Mg^{2+} + 4HCO_3^-$$

References

Al-Yaseri, A., Yekeen, N., Ali, M., et al., 2022. Effect of organic acids on CO_2-rock and water-rock interfacial tension: implications for CO_2 geo-storage. J. Pet. Sci. Eng. 214, 110480. https://doi.org/10.1016/j.petrol.2022.110480.

Ali, M., Jha, N.K., Pal, N., et al., 2022. Recent advances in carbon dioxide geological storage, experimental procedures, influencing parameters, and future outlook. Earth Sci. Rev. 225, 103895. https://doi.org/10.1016/j.earscirev.2021.103895.

Antropov, A., Lavrov, A., Orlic, B., 2017. Effect of in-situ stress alterations on flow through faults and fractures in the cap rock. Energy Proc. 114, 3193–3201. https://doi.org/10.1016/j.egypro.2017.03.1449.

Asem, P., Gardoni, P., 2022. A probabilistic, empirical model for permeability of mudstone. Probab. Eng. Mech. 69, 103291. https://doi.org/10.1016/j.probengmech.2022.103262.

Bachu, S., 2016. Identification of oil reservoirs suitable for CO_2-EOR and CO_2 storage (CCUS) using reserves databases, with application to Alberta, Canada. Int. J. Greenh. Gas Control 44, 152–165. https://doi.org/10.1016/j.ijggc.2015.11.013.

Bachu, S., Adams, J.J., 2003. Sequestration of CO_2 in geological media in response to climate change: capacity of deep saline aquifers to sequester CO_2 in solution. Energy Convers. Manag. 44 (20), 3151–3175. https://doi.org/10.1016/S0196-8904(03)00101-8.

Bachu, S., Bonijoly, D., Bradshaw, J., et al., 2007. CO_2 storage capacity estimation: methodology and gaps. Int. J. Greenh. Gas Control 1 (4), 430–443. https://doi.org/10.1016/S1750-5836(07)00086-2.

Bachu, S., Shaw, J., 2003. Evaluation of the CO_2 sequestration capacity in Alberta's oil and gas reservoirs at depletion and the effect of underlying aquifers. J. Can. Pet. Technol. 42 (9), 51–61. https://doi.org/10.2118/03-09-02.

Bao, X.L., Fragoso, A., Aguilera, R., 2023. Simultaneous enhanced oil recovery, CCUS and UHUS in shale oil reservoirs. Int. J. Coal Geol. 275, 104306. https://doi.org/10.1016/j.coal.2023.104301.

Cao, D.S., Zeng, L.B., Gomez-Rivas, E., 2024. Correction of linear fracture density and error analysis using underground borehole data. J. Struct. Geol. 184, 105152. https://doi.org/10.1016/j.jsg.2024.105152.

Chen, B.W., Wang, R., Li, Q., et al., 2023a. Status and advances of research on caprock sealing properties of CO_2 geological storage. Geol. J. China Univ. 29 (1), 85–99. https://doi.org/10.16108/j.issn1006-7493.2023010 (in Chinese).

Chen, H., Yu, H.Z., Zhou, B., et al., 2023b. Storage mechanism and dynamic characteristics of CO_2 dissolution in saline aquifers. Energy Fuel. 37 (5), 3875–3885. https://doi.org/10.1021/acs.energyfuels.2c03987.

Chen, Q., 2009. Research on Structure Stress and Controlling on Structure in Western Gaoyou Depression of Subei Basin. PhD Thesis. China University of Petroleum (East China).

Chen, X.S., Li, Y.P., Jiang, Y.L., et al., 2022. Theoretical research on gas seepage in the formations surrounding bedded gas storage salt cavern. Pet. Sci. 19 (4), 1766–1778. https://doi.org/10.1016/j.petsci.2022.01.021.

Dar, A.A., Hameed, J., Huo, C., et al., 2022. Recent optimization and panelizing measures for green energy projects; insights into CO_2 emission influencing to circular economy. Fuel 314, 123094. https://doi.org/10.1016/j.fuel.2021.123094.

Dove, P.M., Crerar, D.A., 1990. Kinetics of quartz dissolution in electrolyte solutions using a hydrothermal mixed flow reactor. Geochem. Cosmochim. Acta 54 (4), 955–969. https://doi.org/10.1016/0016-7037(90)90431-J.

Du, Y., Sang, S.X., Wang, W.F., et al., 2018. Experimental study of the reactions of supercritical CO_2 and minerals in high-rank coal under formation conditions. Energy Fuel. 32 (2), 1115–1125. https://doi.org/10.1021/acs.energyfuels.7b02650.

Durham, W.B., Bourcier, W.L., Burton, E.A., 2001. Direct observation of reactive flow in a single fracture. Water Resour. Res. 37 (1), 1–12. https://doi.org/10.1029/2000WR900228.

Edlmann, K., Haszeldine, S., McDermott, C.I., 2013. Experimental investigation into the sealing capability of naturally fractured shale caprocks to supercritical carbon dioxide flow. Environ. Earth Sci. 70 (7), 3393–3409. https://doi.org/10.1007/s12665-013-2407-y.

Elkhoury, J.E., Ameli, P., Detwiler, R.L., 2013. Dissolution and deformation in fractured carbonates caused by flow of CO_2-rich brine under reservoir conditions. Int. J. Greenh. Gas Control 16, S203–S215. https://doi.org/10.1016/j.ijggc.2013.02.023.

Finkbeiner, T., Zoback, M., Flemings, P., et al., 2001. Stress, pore pressure, and dynamically constrained hydrocarbon columns in the South Eugene Island 330 field, Northern Gulf of Mexico. AAPG Bull. 85 (6), 1007–1031. https://doi.org/10.1306/8626CA55-173B-11D7-8645000102C1865D.

Grimm, R.P., Eriksson, K.A., Ripepi, N., et al., 2012. Seal evaluation and confinement screening criteria for beneficial carbon dioxide storage with enhanced coal bed methane recovery in the Pocahontas Basin, Virginia. Int. J. Coal Geol. 90–91, 110–125. https://doi.org/10.1016/j.coal.2011.11.002.

Hao, F., Zhu, W.L., Zou, H.Y., et al., 2015. Factors controlling petroleum accumulation and leakage in overpressured reservoirs. AAPG Bull. 99 (5), 831–858. https://doi.org/10.1306/01021514145.

Hou, L.H., Yu, Z.C., Luo, X., et al., 2022. Self-sealing of caprocks during CO_2 geological sequestration. Energy 252, 124063. https://doi.org/10.1016/j.energy.2022.124064.

Ichikawa, Y., Choi, J.H., Kim, B.C., 2007. Coupled diffusion and seepage problem in porous media. Zairyo 56 (9), 851–857. https://doi.org/10.2472/jsms.56.851.

Ishaq, H., Crawford, C., 2023. CO_2-based alternative fuel production to support development of CO_2 capture, utilization and storage. Fuel 331, 125684. https://doi.org/10.1016/j.fuel.2022.125684.

Ju, W., Sun, W.F., 2016. Tectonic fractures in the Lower Cretaceous Xiagou Formation of Qingxi Oilfield, Jiuxi Basin, NW China. Part two: Numerical simulation of tectonic stress field and prediction of tectonic fractures. J. Pet. Sci. Eng. 146, 626–636. https://doi.org/10.1016/j.petrol.2016.05.002.

Ju, W., Wang, J.L., Fang, H.H., et al., 2019. Paleotectonic stress field modeling and prediction of natural fractures in the Lower Silurian Longmaxi shale reservoirs, Nanchuan region, South China. Mar. Petrol. Geol. 100, 20–30. https://doi.org/10.1016/j.marpetgeo.2018.10.052.

Khatri, R.A., Chuang, S.S.C., Soong, Y., et al., 2006. Thermal and chemical stability of regenerable solid amine sorbent for CO_2 capture. Energy Fuel. 20 (4), 1514–1520. https://doi.org/10.1021/ef050402y.

Kurnosov, V.B., Sakharov, B.A., Geptner, A.R., et al., 2020. Clay minerals in basalt sills from the sediment cover, East Pacific Rise. Lithol. Miner. Resour. 55 (2), 152–163. https://doi.org/10.1134/S0024490220020042.

Laubach, S.E., 2003. Practical approaches to identifying sealed and open fractures. AAPG Bull. 87 (4), 561–579. https://doi.org/10.1306/11060201106.

Laubach, S.E., Lander, R.H., Criscenti, L.J., et al., 2019. The role of chemistry in fracture pattern development and opportunities to advance interpretations of geological materials. Rev. Geophys. 57 (3), 1065–1111. https://doi.org/10.1029/2019RG000671.

Lavrov, A., 2016. Dynamics of stresses and fractures in reservoir and cap rock under production and injection. Energy Proc. 86, 381–390. https://doi.org/10.1016/j.egypro.2016.01.039.

Li, S.Y., Wang, P., Wang, Z.J., et al., 2023a. Strategy to enhance geological CO_2 storage capacity in saline aquifer. Geophys. Res. Lett. 50 (3), e2022GL101431. https://doi.org/10.1029/2022GL101431.

Li, Y., Wang, R., Zhao, Q.M., et al., 2023b. A CO_2 storage potential evaluation method for saline aquifers in a petroliferous basin. Petrol. Explor. Dev. 50 (2), 484–491. https://doi.org/10.1016/S1876-3804(23)60403-3.
Li, Z.W., Dong, M.Z., Li, S.L., et al., 2006. CO_2 sequestration in depleted oil and gas reservoirs—caprock characterization and storage capacity. Energy Convers. Manag. 47 (11–12), 1372–1382. https://doi.org/10.1016/j.enconman.2005.08.023.
Liu, C., Xie, Q.B., Wang, G.W., et al., 2016. Reservoir properties and controlling factors of contact metamorphic zones of the diabase in the northern slope of the Gaoyou Sag, Subei Basin, eastern China. J. Nat. Gas Sci. Eng. 35, 392–411. https://doi.org/10.1016/j.jngse.2016.08.070.
Liu, H.C., Lu, H., Hu, H., 2024. CO_2 capture and mineral storage: state of the art and future challenges. Renew. Sustain. Energy Rev. 189, 113908. https://doi.org/10.1016/j.rser.2023.113908.
Liu, Y., Chen, Q.H., Wang, X., et al., 2017. Influence of normal fault growth and linkage on the evolution of a rift basin: a case from the Gaoyou depression of the Subei Basin, eastern China. AAPG Bull. 101 (2), 265–288. https://doi.org/10.1306/06281615008.
Liu, Z.X., Gao, M., Zhang, X.M., et al., 2023. CCUS and CO_2 injection field application in abroad and China: Status and progress. Geoenergy Sci. Eng. 229, 212011. https://doi.org/10.1016/j.geoen.2023.212011.
Ma, C.F., Lin, C.Y., Dong, C.M., et al., 2020. Quantitative relationship between argillaceous caprock thickness and maximum sealed hydrocarbon column height. Nat. Resour. Res. 29 (3), 2033–2049. https://doi.org/10.1007/s11053-019-09554-w.
Mao, Z., Zeng, L.B., Liu, G.P., et al., 2020. Characterization and effectiveness of natural fractures in deep tight sandstones at the south margin of the Junggar Basin, northwestern China. Oil Gas Geol. 41 (6), 1212–1221. https://doi.org/10.11743/ogg20200609 (in Chinese).
Pham, V.T.H., Lu, P., Aagaard, P., et al., 2011. On the potential of CO_2-water-rock interactions for CO_2 storage using a modified kinetic model. Int. J. Greenh. Gas Control 5 (4), 1002–1015. https://doi.org/10.1016/j.ijggc.2010.12.002.
Qin, J., Zhong, Q.H., Tang, Y., et al., 2022. CO_2 storage potential assessment of offshore saline aquifers in China. Fuel 341, 127681. https://doi.org/10.1016/j.fuel.2023.127681.
Qiu, Y.F., 2022. Comprehensive evaluation of medium-shallow caprocks conditions in deep depression zone of Gaoyou Sag. Complex Hydrocarb. Reserv. 15 (1), 8–12 (in Chinese).
Quaye, J.A., Jiang, Z.X., Liu, C., et al., 2022. Biogenically modified reservoir rock quality: a case from the lowermost member Paleocene Funing Formation, Gaoyou Depression, Subei Basin, China. J. Pet. Sci. Eng. 219, 111126. https://doi.org/10.1016/j.petrol.2022.111126.
Quaye, J.A., Jiang, Z.X., Zhou, X.W., 2019. Bioturbation influence on reservoir rock quality: a case study of well Bian-5 from the second member Paleocene Funing Formation in the Jinhu Sag, Subei Basin, China. J. Pet. Sci. Eng. 172, 1165–1173. https://doi.org/10.1016/j.petrol.2018.09.026.
Rohmer, J., Pluymakers, A., Renard, F., 2016. Mechano-chemical interactions in sedimentary rocks in the context of CO_2 storage: Weak acid, weak effects? Earth Sci. Rev. 157, 86–110. https://doi.org/10.1016/j.earscirev.2016.03.009.
Rosenbauer, R.J., Koksalan, T., Palandri, J.L., 2005. Experimental investigation of CO_2-brine-rock interactions at elevated temperature and pressure: Implications for CO_2 sequestration in deep-saline aquifers. Fuel Process. Technol. 86 (14–15), 1581–1597. https://doi.org/10.1016/j.fuproc.2005.01.011.
Rui, Z.H., Zeng, L.B., Dindoruk, B., 2025. Challenges in the large-scale deployment of CCUS. Engineering 44, 17–20. https://doi.org/10.1016/j.eng.2024.11.031.
Rutqvist, J., Tsang, C.F., 2002. A study of caprock hydromechanical changes associated with CO_2-injection into a brine formation. Environ. Geol. 42 (2–3), 296–305. https://doi.org/10.1007/s00254-001-0499-2.
Sakthivel, S., Yekeen, N., Theravalappil, R., et al., 2024. Influence of carbon nanodots on the carbonate/CO_2/brine wettability and CO_2-brine interfacial tension: Implications for CO_2 geo-storage. Fuel 355, 129404. https://doi.org/10.1016/j.fuel.2023.129404.
Sennaoui, B., Ling, K., Ostadhassan, M., et al., 2025. Subsurface CO_2 storage in unconventional reservoirs: Insights into pore-scale characterization of geochemical interactions and particle migration. Geoenergy Sci. Eng. 247, 213688. https://doi.org/10.1016/j.geoen.2025.213688.
Smith, D.A., 1966. Theoretical considerations of sealing and non-sealing faults. AAPG Bull. 50 (2), 363–374. https://doi.org/10.1306/5D25B48F-16C1-11D7-8645000102C1865D.
Song, J., Zhang, D.X., 2013. Comprehensive review of caprock-sealing mechanisms for geologic carbon sequestration. Environ. Sci. Technol. 47 (1), 9–22. https://doi.org/10.1021/es301610p.
Su, A., Chen, H.H., Feng, Y.X., et al., 2022. Multistage fracturing history in the Paleocene lacustrine shale oil reservoirs of the Subei Basin, Eastern China. Mar. Petrol. Geol. 144, 105835. https://doi.org/10.1016/j.marpetgeo.2022.105835.
Tremosa, J., Mito, S., Audigane, P., et al., 2017. Experimental assessment of well integrity for CO_2 geological storage: a numerical study of the geochemical interactions between a CO_2-brine mixture and a sandstone-cement-steel sample. Appl. Geochem. 78, 61–73. https://doi.org/10.1016/j.apgeochem.2016.12.011.
Wang, X.Z., Zeng, F.H., Gao, R.M., et al., 2017. Cleaner coal and greener oil production: an integrated CCUS approach in Yanchang Petroleum Group. Int. J. Greenh. Gas Control 66, 13–22. https://doi.org/10.1016/j.ijggc.2017.04.001.
Watson, M.N., Zwingmann, N., Lemon, N.M., 2004. The Ladbroke Grove–Katnook carbon dioxide natural laboratory: a recent CO_2 accumulation in a lithic sandstone reservoir. Energy 29 (9–10), 1457–1466. https://doi.org/10.1016/j.energy.2004.03.079.
Wu, W., Zoback, M.D., Kohli, A.H., 2017. The impacts of effective stress and CO_2 sorption on the matrix permeability of shale reservoir rocks. Fuel 203, 179–186. https://doi.org/10.1016/j.fuel.2017.04.103.
Xu, T.F., Apps, J.A., Pruess, K., 2003. Numerical simulation to study mineral trapping for CO_2 disposal in deep aquifers. Appl. Geochem. 19 (6), 917–936. https://doi.org/10.1016/j.apgeochem.2003.11.003.
Yang, J.F., Yang, C.H., Gu, Q.Y., et al., 2023. Economic evaluation and influencing factors of CCUS-EOR technology: a case study from a high water-bearing oilfield in Xinjiang, China. Energy Rep. 10, 153–160. https://doi.org/10.1016/j.egyr.2023.06.013.
Yekeen, N., Padmanabhan, E., Sevoo, T.A., et al., 2020. Wettability of rock/CO_2/brine systems: a critical review of influencing parameters and recent advances. J. Ind. Eng. Chem. 88, 1–28. https://doi.org/10.1016/j.jiec.2020.03.021.
Yu, Z.C., Liu, L., Yang, S.Y., et al., 2012. An experimental study of CO_2-brine-rock interaction at *in situ* pressure-temperature reservoir conditions. Chem. Geol. 326–327, 88–101. https://doi.org/10.1016/j.chemgeo.2012.07.030.
Zeng, L.B., 2008. Formation and Distribution of Fractures in low-permeability Sandstone Reservoirs. Science Press, Beijing (in Chinese).
Zeng, L.B., Gong, L., Zhang, Y.Z., et al., 2023. A review of the genesis, evolution, and prediction of natural fractures in deep tight sandstones of China. AAPG Bull. 107 (10), 1687–1721. https://doi.org/10.1306/07052322120.
Zeng, L.B., Ke, S.Z., Liu, Y., 2010. Fracture Study Methods for Low Permeability Oil and Gas Reservoir. Petroleum Industry Press, Beijing (in Chinese).
Zeng, L.B., Li, X.Y., 2009. Fractures in sandstone reservoirs with ultra-low permeability: a case study of the Upper Triassic Yanchang Formation in the Ordos Basin, China. AAPG Bull. 93 (4), 461–477. https://doi.org/10.1306/09240808047.
Zeng, L.B., Qi, J.F., Wang, C.G., et al., 2008. The influence of tectonic stress on fracture formation and fluid flow. Earth Sci. Front. 15 (3), 292–298 (in Chinese).
Zeng, L.B., Qi, J.F., Wang, Y., 2007. Origin type of tectonic fractures and geological conditions in low-permeability reservoirs. Acta Pet. Sin. 28 (4), 52–56 (in Chinese).
Zeng, L.B., Su, H., Tang, X.M., et al., 2013. Fractured tight sandstone oil and gas reservoirs: a new play type in the Dongpu depression, Bohai Bay Basin, China. AAPG Bull. 97 (3), 363–377. https://doi.org/10.1306/09121212057.
Zeng, L.B., Tang, X.M., Wang, T.C., et al., 2012. The influence of fracture cements in tight Paleogene saline lacustrine carbonate reservoirs, Western Qaidam Basin, northwest China. AAPG Bull. 96 (11), 2003–2017. https://doi.org/10.1306/04181211090.
Zeng, L.B., Xu, X., Ma, S.J., et al., 2024. Contribution of lamellation fractures to porosity and permeability of shales: a case study of the Jiaoshiba area in the Sichuan Basin, China. Geoenergy Sci. Eng. 232, 212439. https://doi.org/10.1016/j.geoen.2023.212439.
Zhang, G.Y., Lu, P., Zhang, Y.L., et al., 2015. Effects of rate law formulation on predicting CO_2 sequestration in sandstone formations. Int. J. Energy Res. 39 (14), 1890–1908. https://doi.org/10.1002/er.3374.
Zhang, K., Sang, S.X., Zhou, X.Z., et al., 2021a. Influence of supercritical CO_2-H_2O-caprock interactions on the sealing capability of deep coal seam caprocks related to CO_2 geological storage: a case study of the silty mudstone caprock of coal seam no. 3 in the Qinshui Basin, China. Int. J. Greenh. Gas Control 106, 103282. https://doi.org/10.1016/j.ijggc.2021.103282.
Zhang, Y.Z., Zeng, L.B., Luo, Q., et al., 2021b. Influence of natural fractures on tight oil migration and production: a case study of Permian Lucaogou Formation in Jimsar Sag, Junggar Basin, NW China. J. Earth Sci. 32 (4), 927–945. https://doi.org/10.1007/s12583-021-1442-y.
Zhao, J.Z., Wang, L.L., Wei, B., et al., 2025. CO_2 utilization and geological storage in unconventional reservoirs after fracturing. Engineering 48, 92–106. https://doi.org/10.1016/j.eng.2025.01.005.
Zheng, X.J., Espinoza, D.N., 2021. Multiphase CO_2-brine transport properties of synthetic fault gouge. Mar. Petrol. Geol. 129, 105054. https://doi.org/10.1016/j.marpetgeo.2021.105054.
Zhu, Q.L., Chen, D.B., Gong, Y.J., et al., 2023a. Analysis of CO_2 geological storage condition in Jiangsu Province and offshore area. Geol. J. China Univ. 29 (1), 25–36. https://doi.org/10.16108/j.issn1006-7493.2022080 (in Chinese).
Zhu, X., Duan, H., Sun, Y., 2023b. Break through and significance of Paleogene continental shale oil exploration in Gaoyou Sag, Subei Basin. Acta Pet. Sin. 44 (8), 1206–1221 (in Chinese).
Zhu, Z.H., Li, M.Y., Lin, M.Q., et al., 2011. Review of the CO_2-water-rock interaction in reservoir. Bull. China Soc. Mineral Petrol. Geochem. 30 (1), 104–112 (in Chinese).